Università degli Studi di Napoli Federico II

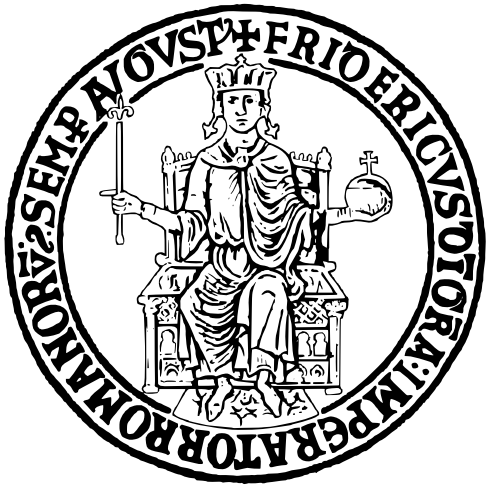

Scuola Politecnica e delle Scienze di Base
Dipartimento di Ingegneria Industriale

Corso di Laurea in Ingegneria Aerospaziale
Classe delle Lauree in Ingegneria Industriale (L-9)

Elaborato di Tesi in Meccanica del Volo

Static stability analysis of wing-body configurations of the airplanes included in JPAD Modeller

Relatore:
Prof. Danilo Ciliberti

Candidato:
Antonio Dario Marotta
N35/3678

Anno Accademico 2022 - 2023

Summary

1 Introduction **6**

2 Geometric and Aerodynamic Modelling **7**
2.1 Aircraft Geometry 7
2.2 Exporting the Aircraft 10
2.3 Vortex Lattice Method 11
2.4 Calculation of the Aerodynamic Centre Position of the Wing 14
2.4.1 Analysis the Isolated Wing 14
2.4.2 Evaluation of the Wing Aerodynamic Centre 15
2.5 Evaluating the Aerodynamic Derivatives 16
2.5.1 Wing 16
2.5.2 Isolated Fuselage 18
2.5.3 Wing and Body 19
2.6 Discussion of Results 20

3 Semi-Empirical Methods and Results Comparison **21**
3.1 Munk Theory for Isolated Body Derivatives 21
3.2 Multhopp Method for Body with Wing Effects 25

4 Conclusions **30**

List of Figures

2.1 Definition of TABLE 1 dimensions 8
2.2 Definition of JPAD interface where data can be found 8
2.3 Definition of BRF and CRF 9
2.4 Definitions of Horizontal Tail and Wing dimensions 9
2.5 Comparison between JPAD and OpenVSP geometries 10
2.6 The velocity field induced by a vortex of positive *(right)* and negative *(left)* circulation . 11
2.7 The velocity field induced by a ring vortex 12
2.8 Scheme of the discretization used by VSPAERO and visualization of the results 13
2.9 Options for running an analysis with VSPAERO 14
2.10 Results from VSPAERO for the wing of the A220-300 14
2.11 Relating the moment around pole B to the moment around pole A 15
2.12 Comparison among the moments taken at three points for the A220-300 16
2.13 Example of the results file 16
2.14 Differences among C_{M_B} values for an ATR-42 evaluated at three different points 17
2.15 Results for the pitching moment of a G400 with the default grid from JPAD 18
2.16 The same results for the G400 with a finer grid 18
2.17 Differences among $C_{\mathcal{N}_B}$ values for an ATR-42 evaluated at three different points 19
2.18 Visualization of the grid for a wing-body configuration of an ATR-42 19
2.19 Visualization of the grid for a fuselage of an ATR-42 19
2.20 Effects of the Dihedral angle with respect to rolling 20
2.21 Effects on yawing and rolling associated with a sweep angle 20

3.1 Momentum orientation in the three cases described (for a detailed explanation of the matrix see Reference [9]) 24
3.2 Moment orientation for a current with angle of attack and sideslip 24
3.3 Definition of the arbitrary plane along the x-axis 25
3.4 Value for the wing upwash gradient evaluated for a wing of $\mathcal{AR} = 8$ and $C_{L_\alpha} = 4.5$ rad^{-1} [1] 27
3.5 Table of values of $k_2 - k_1$ 27
3.6 Flow chart for the program implementing the Munk method for evaluating $C_{M_{\alpha,B}}$ 28
3.7 Flow chart for the program implementing the Multhopp method for evaluating $C_{M_{\alpha,B(W)}}$. 29

List of Tables

2.1 Definition of Reference Measures 7

A1 Positions of the Wing reference measurements A1
A2 Positions of the Horizontal Tail reference measurements A2
A3 Values the lift and moment coefficients and the positions of the wing aerodynamic centre for the isolated wing A3
A4 Values of longitudinal and latero-directional stability derivatives for the isolated wings (all coefficients are expressed in deg^{-1}) A4
A5 Values of longitudinal and latero-directional stability derivatives in deg^{-1} for the wing-body configuration A5
A6 Values of longitudinal and latero-directional stability derivatives in deg^{-1} for the isolated fuselage obtained from VSPAERO A6
A7 Comparison among results from the Munk method and VLM on isolated fuselage A7
A8 Comparison among results from the Multhopp method and VLM (in deg^{-1}) on the body under the aerodynamic interference of the wing A8
A9 Values of $C_{M_{\text{W}}}$ in deg^{-1} at different angles of attack A9

Abstract

The scope of this thesis is to analyse the stability behaviour for several planes included in the JPAD virtual hangar. For each plane different configurations are studied, namely the isolated wing, isolated fuselage, and wing-body configuration, using the linear vortex lattice solver VSPAERO, which is an OpenVSP tool. Then these results are compared with the ones obtained from semi-empirical methods like the Munk-Multhopp methods. This work provides a collection of stability derivatives of wing, fuselage, and wing-body combinations of in-service transport aircraft. It also shows that the results of the VSPAERO aerodynamic solver are in good agreement with those calculated with semi-empirical methods.

Sommario

Questa tesi si pone l'obiettivo di analizzare la stabilità dei vari velivoli inclusi nel virtual hangar di JPAD. Per ogni velivolo vengono studiate diverse configurazioni, quali l'ala, la fusoliera e la configurazione ala-fusoliera, usando il solutore aerodinamico VSPAERO, incluso nella suite OpenVSP. Successivamente, i risultati sono confrontati con quelli ottenuti tramite l'applicazione di metodi semi-empirici come quelli di Munk-Multhopp. Questo lavoro fornisce una raccolta di derivate di stabilità per ali, fusoliere e combinazioni di ala e fusoliera per vari velivoli da trasporto attualmente in servizio. Viene inoltre mostato che i risultati ottenuti dal risolutore VSPAERO sono in accordo con quelli ricavati dai suddetti metodi empirici.

Chapter 1

Introduction

The behaviour of an aircraft when it is subjected to perturbations from its equilibrium position is a fundamental information to know. In other words, it must be known what effect will have on the airplane the system of aerodynamic actions that it will be experienced after a variation of angle of attack or sideslip. For small variations of parameters, such as flight (e.g., angle of attack, sideslip, Mach number) or input parameters (e.g., the results of the action of the pilot), a linear relation between such parameters and forces (moments) can be assumed. It follows that the stability of a complete aircraft will be a linear combination of effects caused by the wing, body, and the control surfaces such as the elevator for the longitudinal stability. Components like the horizontal and vertical tail are employed to stabilize the wing-body system that is usually unstable, thus it is necessary to have an estimation of the instability of this system, in order to choose the right parameters for these surfaces to make the whole system stable and trimmable.
The hypothesis of small variations of parameters allows to consider linear relations between the angles of attack and sideslip (flight parameters) and coefficients like lift and moment, meaning that linearised theories (cf. Reference [1]) can be employed to have an esteem of these coefficients that are necessary to understand the stability behaviour.
A numerical method for obtaining the required coefficients is the Vortex Lattice Method, or VLM, that, under the assumption of irrotational and inviscid fluid, allows to build an algebraic system of equations whose solution gives the circulation of the fluid around the inspected part (cf. Reference [2]). From the circulation it is possible to estimate lift and moment coefficients. These results can be compared the ones obtained with other methods, relying on the same assumptions on the flow (otherwise the results could not be compared), to obtain the aerodynamic forces and moments acting on parts of the vehicle.
Fuselages play an important role in the stability of the vehicle, since they present an unstable behaviour both in longitudinal and latero-directional dynamics. A fuselage is essentially an elongated, non-axisymmetric body that does not generate any lift. The asymmetric pressure distribution generates a free couple that is the cause of the aerodynamic instability. These effects, for an isolated fuselage, can be easily studied supposing that the body is slender so that the flow at a position along the fuselage can be considered bi-dimensional, adding then a corrective factor for its finite slenderness (cf. References [1, 3, 4]).
When the wing is mounted on the fuselage, the interference of one element on the other alters the behaviour of both components significantly: for example, taking as reference point the wing aerodynamic centre (cf. Reference [1]), a wing-body configuration will have a varying moment coefficient with the angle of attack, while for the isolated wing it will be constant. As for the isolated fuselage, the influence of the wing on the fuselage can be computed using a semi-empirical method. Results from the VLM can be compared with the ones obtained from this method since the effects of the wing-body system can be, at a first approximation, considered as the sum of the effects of the wing alone plus the effects of the fuselage due to the presence of the wing. In this way VLM gives the global results for the wing and body configuration, whereas the semi-empirical method gives the effect of the fuselage under the influence of the wing, so that a comparison between these results can be made.

Chapter 2

Geometric and Aerodynamic Modelling

2.1 Aircraft Geometry

The JPAD software has been used to obtain data representing the aircraft geometry, such as the wing span, planform surface, mean aerodynamic chord and so on.
JPAD Modeller is a parametric CAD software which is capable of generating simple models from overall geometric and operational data using other aircraft specifications from its database, allowing to refine it afterward (cf. Reference [5]).
The data obtained from JPAD can be divided roughly in two categories being:

- the reference measures, like the mean aerodynamic chord, the planform area, the wing span and so on;
- the geometry required by the linear vortex solver VSPAERO to conduct the analysis.

The first ones are used to make the moment and lift nondimensional obtaining the corresponding coefficients, while the latter are used by both VSPAERO and MATLAB to get the results of the semi-empirical methods which will be introduced hereafter. The first three measures are (see FIGURE 2.1):

- $\bar{c}$ is the mean aerodynamic chord;
- S_{ref} is the planform surface of the wing;
- b_{ref} is the wing span.

	Aircraft	$\bar{c}$ (m)	S_{ref} (m)	b_{ref} (m)
1	A220-300	3.87	111.95	35.01
2	A320neo	3.98	122.6	35.8
3	A340	8.09	437.3	63.45
4	AN32	2.81	73.69	28.79
5	ATR42	2.29	54.5	24.57
6	ATR72	2.32	61	27.05
7	B737-600	4.47	124.6	34.3
8	B737-700	4.47	125.12	34.44
9	B737-800	4.47	125.12	34.44
10	B737-900	4.47	125.12	34.44
11	C-130H	4.52	154.98	34.7
12	C-27J	2.82	57.13	21.22
13	Canadair CL415	3.51	100.33	28.6
14	EmbraerLegacy650	2.8	51	21.15
15	Falcon10x	4.09	122.01	33.6
16	Falcon8x	3.2	70.75	26.28
17	G400	4.29	98.96	26.3
18	G650	4.48	119.2	30.36
19	G700	4.19	119.28	31.39
20	G800	4.38	119.2	31.39
21	global6000	3.86	94.78	28.69
22	global7000	4.35	122.3	31.77
23	global8000	4.36	122.23	31.75
24	Learjet45	2.14	28.95	14.58
25	Praetor600	2.39	44.67	21.42
26	Q400	2.44	67.27	28.4
27	Regional Jet RM	4.02	118.58	33.81

Table 2.1: Definition of Reference Measures

These are summarised in TABLE 2.1 and can be found in Jpad interface as shown in FIGURE 2.2. There is necessity to define a pole around which the moments have to be calculated, but this decision is strongly dependent on the choice of an adequate reference frame: both JPAD and OpenVSP use a constructive reference frame (CRF), whose origin is at the tip of the nose of the fuselage, x-axis runs along the fuselage pointing to the tail, y-axis points at the right of the pilot, and z-axis is obtained so that $\{x, y, z\}$ is a left handed coordinate system. This means that all the coordinates reported in TABLE A1 and TABLE A2 are defined in such reference frame.

Instead derivatives are expressed in a body reference frame (BRF), whose axes are parallel to the previous ones but with different orientation:

- the BRF x-axis is parallel to CRF x-axis but it points in the opposite direction, from the tail to the nose;
- y-axis coincides with the y-axis of the CRF;
- z-axis happens to be anti-parallel to the CRF z-axis, pointing downward, because both systems are left handed.

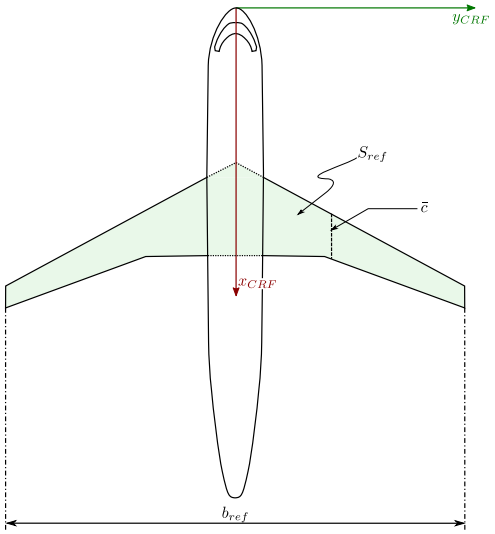

Figure 2.1: Definition of TABLE 1 dimensions

Last but not least, BRF is a baricentric reference frame, meaning that it has its origin in the airplane centre of mass, while CRF is not. FIGURE 2.3 shows these two Reference Frames. To get a fair comparison among the different aircraft investigated, the reference point for the moments has been fixed at a quarter of the mean aerodynamic chord, along the x_{CRF} axis and at the z coordinate of the wing apex. The leading edge of the mean aerodynamic chord is obtained from JPAD in a different reference frame, that is derived from the body reference frame through an x and z translation at the wing apex, as shown in FIGURE 2.4. The new quantities introduced are:

- X_{le}, Z_{le} are the (x, z) coordinates of wing apex in the Constructive Reference Frame;
- $x_{\bar{c}}$, $z_{\bar{c}}$ are the (x, z) coordinates of $\bar{c}$ leading edge, in a reference frame whose axis are parallel to the Constructive Reference Frame and its origin in the wing apex.

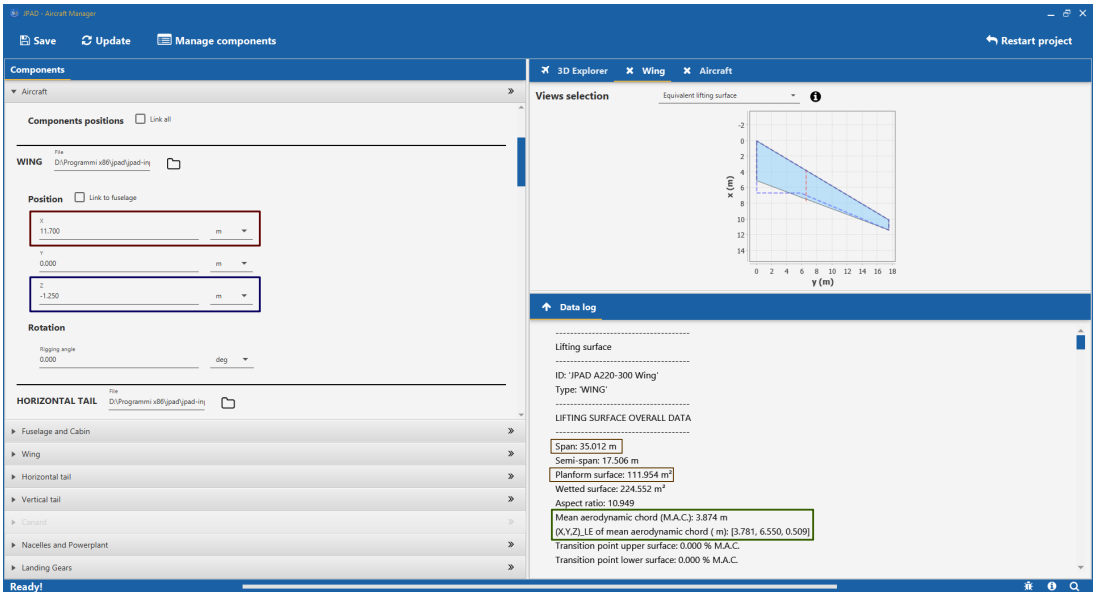

Figure 2.2: Definition of JPAD interface where data can be found

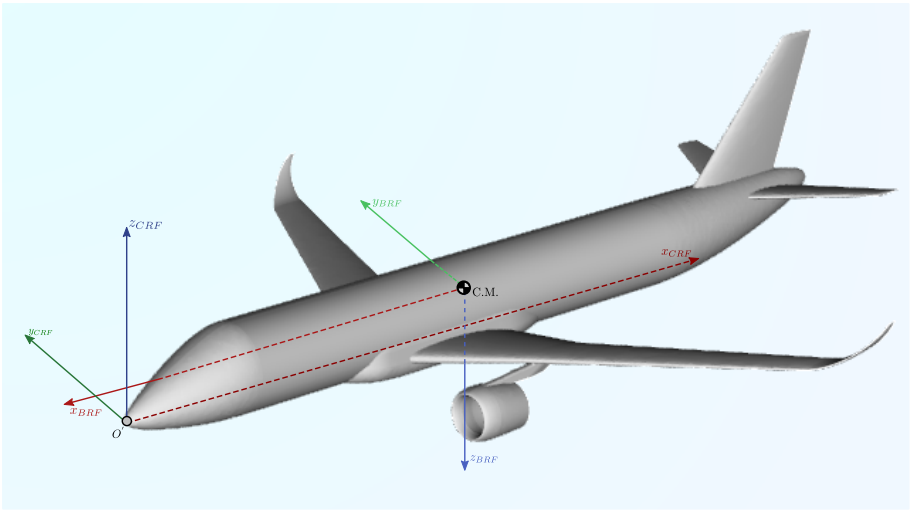

Figure 2.3: Definition of BRF and CRF

Other geometrical data are needed, particularly the ones concerning the horizontal tailplane as they will be required by the semi-empirical methods. These new quantities are:

- $X_{\mathrm{H,le}}$, $Z_{\mathrm{H,le}}$ are the (x, z) coordinates of horizontal tail apex in the CRF;
- $x_{\mathrm{H},\bar{c}}$, $z_{\mathrm{H},\bar{c}}$ are the (x, z) coordinates of the mean aerodynamic chord leading edge of the horizontal tail in a reference frame whose axis are parallel to the CRF with its origin at the horizontal tail apex;
- $\bar{c}_{\mathrm{H}}$ is the mean aerodynamic chord of the horizontal tailplane.

FIGURE 2.4 shows the aforementioned quantities that are also listed in TABLE A2. It is seen these quantities are defined in the same way as the ones reported in Table A1.

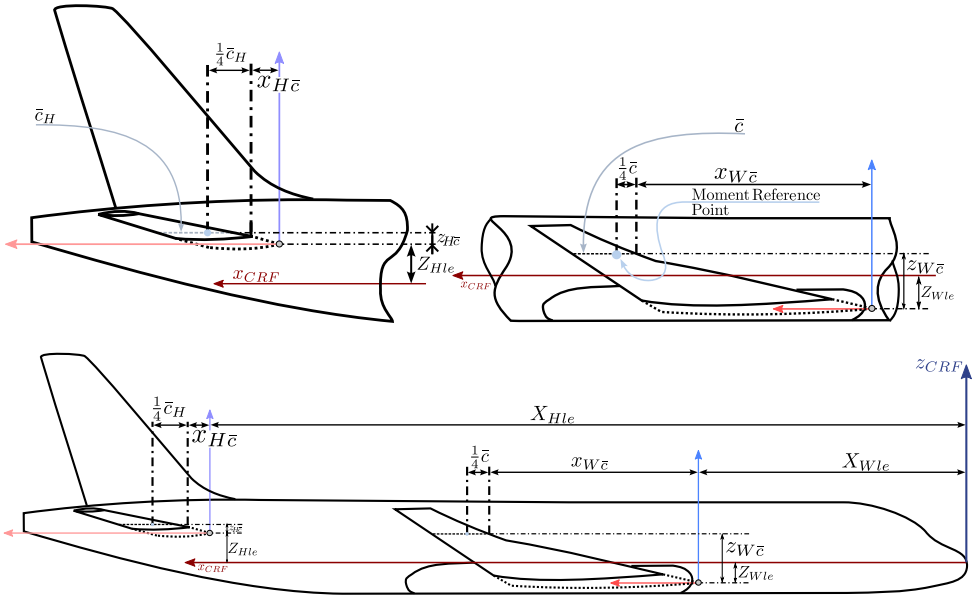

Figure 2.4: Definitions of Horizontal Tail and Wing dimensions

2.2 Exporting the Aircraft

It is necessary to export the geometry from JPAD into a file suitable for OpenVSP.
OpenVSP is an open-source parametric developed by NASA, which, through its tools, is also capable of conducting aerodynamic and structural simulations. The tool used in this thesis is VSPAERO, which conducts analysis employing vortex lattice method.
The standard for OpenVSP takes as input files with `.vsp3` extension, in order to load and analyse the aircraft correctly. This is also an export format supported by JPAD.
The computational grid, once exported from JPAD and imported to OpenVSP, can be tweaked directly into the latter, changing, for example, the number of subdivision along the wing span, or the number of sections in which the fuselage is subdivided. Comparison between JPAD and OpenVSP geometry visualization is shown in FIGURE 2.5. Other further modifications can be made to the aircraft geometry in OpenVSP such as changing the airfoils at specific sections in the wing or changing the relative positions among components.

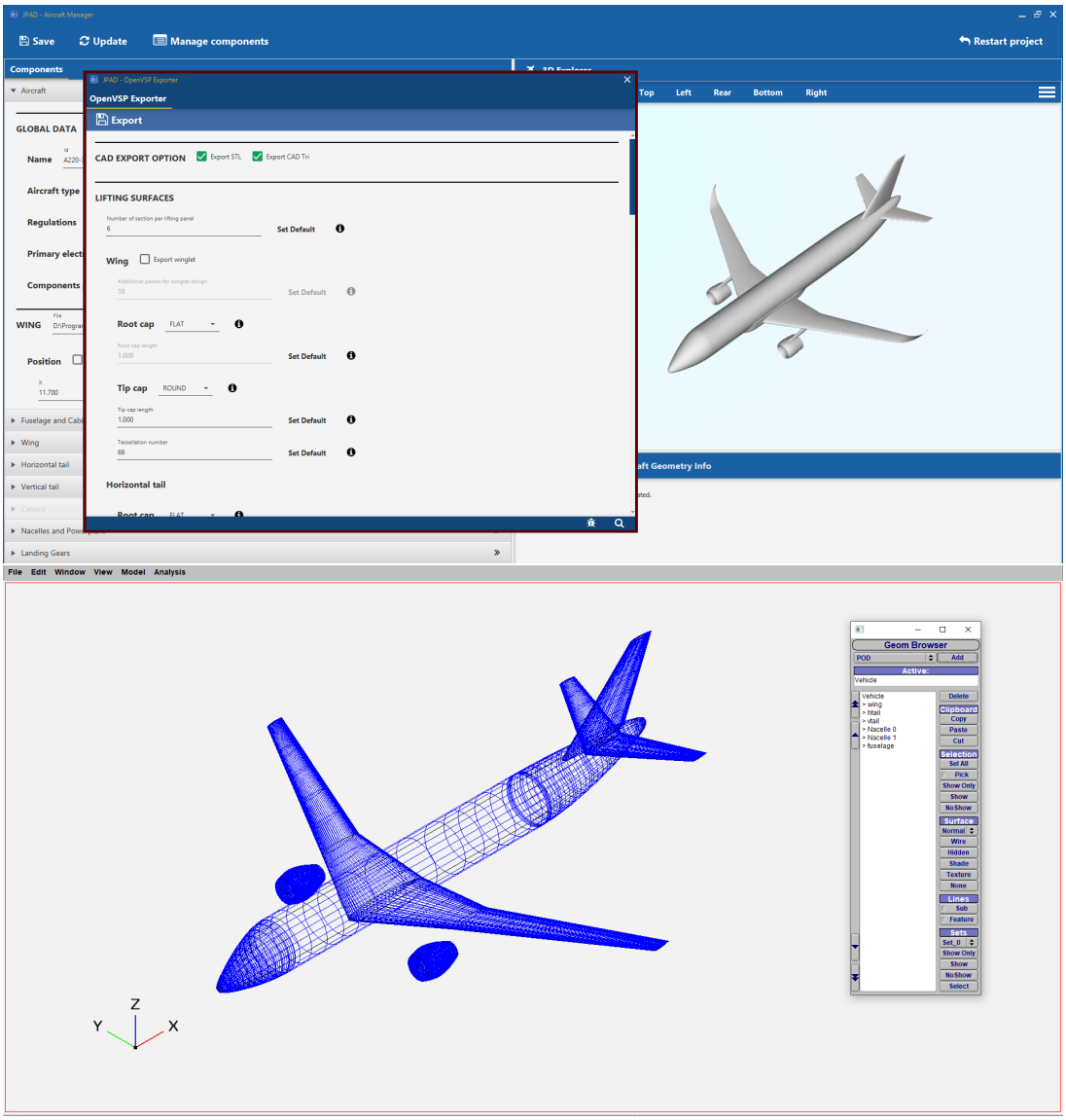

Figure 2.5: Comparison between JPAD and OpenVSP geometries

2.3 Vortex Lattice Method

It has been stated that VSPAERO evaluates lift and moments using the vortex lattice method, thus it is appropriate to give a brief introduction about this method and how it is implemented.
Considering a steady and irrotational flow field, the following two relations are obtained:

$$\nabla \cdot (\rho \mathbf{V}) = 0 \rightarrow \nabla \cdot \mathbf{V} = 0 \qquad \text{if the flow is also incompressible} \tag{2.1}$$

$$\nabla \times \mathbf{V} = \mathbf{0} \tag{2.2}$$

The second relation states that the velocity field is irrotational, hence there must exist a scalar function Φ defined such as:

$$\nabla \Phi = \mathbf{V} \tag{2.3}$$

Substituting this relation into the continuity equation, it yields:

$$\nabla \cdot (\nabla \Phi) = 0 \leftrightarrow \nabla^2 \Phi = 0 \tag{2.4}$$

It has been obtained that the potential function Φ is the solution of the Laplace's equation [2]. This is a second order partial differential equation and it must be paired with two boundary conditions (BCs) dictated by the Physics of the problem. These BCs are:

$$\mathbf{V} \cdot \mathbf{n} = 0 \qquad \text{the fluid is tangent to the body (it cannot pass through it)} \tag{2.5a}$$

$$\lim_{\mathbf{r} \to \infty} \mathbf{V} = \mathbf{V}_\infty \qquad \text{far away from the body the current is undisturbed} \tag{2.5b}$$

Because of the linearity Laplace's equation, the principle of superposition is valid. The flow field can be seen as the summation of the potential function describing the undisturbed current stream Φ_∞ plus the potential of the disturbed velocity profile caused by the presence of the wing Φ^*.
It is now necessary to find some elementary functions that satisfy both the Laplace's equation and (2.5b). This last requirement is motivated by the fact that this kind of functions is used to model the body disturbance in the field, meaning that this disturbance is reduced as the distance from the body is increased, going to zero when the distance goes to infinity.
There are many possible functions that can satisfy the Laplace's equation but, for the sake of the discussion, it will be introduced only the one used in VSPAERO: the vortex singularity. The potential function Φ expressed in Cartesian coordinates for a vortex located at (x_0, z_0) is:

$$\Phi = -\frac{\Gamma}{2\pi} \tan^{-1} \frac{z - z_0}{x - x_0} \tag{2.6}$$

The same function assumes the following form when expressed in polar coordinates with origin in the vortex itself:

$$\Phi = -\frac{\Gamma}{2\pi}\theta \rightarrow V_\theta = \frac{1}{r}\frac{\partial \Phi}{\partial \theta} = -\frac{\Gamma}{2\pi r} \tag{2.7}$$

From the last relation it can be seen that the potential introduced automatically satisfies (2.5b), meaning that the velocity disturbance induced by a vortex tends to zero when the distance from it increases.
Using the principle of superposition, the disturbance caused by a lifting body can me modelled as a distribution of $\{\Phi\}_i$ vortices, whose linear combination must satisfy (2.5a) (as (2.5b) is automatically satisfied).
In a three dimensional case the vortex has to be closed or it has to have its starting and ending points at infinity, because from Helmholtz theorems [2] its vorticity — defined as the flux of the rotor of the velocity vector V through a section of the vortex tube — must be constant, and this could not be possible if the vortex tube had to end abruptly (in

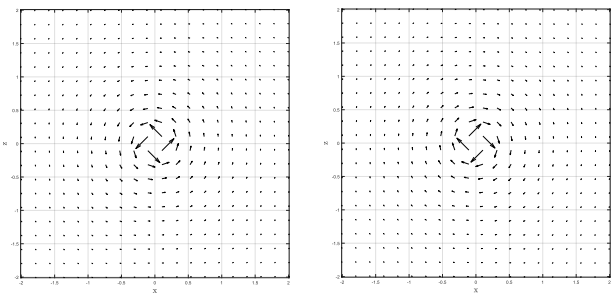

Figure 2.6: The velocity field induced by a vortex of positive *(right)* and negative *(left)* circulation

that case the flux of the last surface would be zero). Based on this requirement a wing can be modelled as a distribution of horseshoe vortices or as a distribution of ring vortices. OpenVSP uses the second kind of vortex structure in its tool VSPAERO.
The vortex lattice method, implemented by VSPAERO, discretizes the wing into a series of flat plates, and in each one of these places a ring vortex of fixed intensity Γ_j (cf. Reference [6]). The leading vortex segment is placed at a quarter of the panel chord (because it is the position of the centre of pressure for a flat plate), while the collocation point is defined at three quarters. The collocation point for a panel is the point where the boundary condition must be specified. Since every panel is represented only by a single vortex, the BC can be enforced only in a single point. The BC (2.5a) becomes:

$$(\mathbf{V}_\infty - \mathbf{V}_j) \cdot \mathbf{n} = 0 \qquad\qquad j = 1, ...m$$

where V_j is the velocity induced by all the ring vortices at the j-th control point and m is the number of panels the wing has been discretized in.
The induced velocity induced by the i-th circular vortex of each panel in the j-th point P_j is obtained using the Biot-Savart law [2]:

$$\mathbf{V}_{ij} = \underbrace{\frac{\Gamma_i}{4\pi} \sum_{k=1}^{4} \int_{x_k}^{x_{k+1}} \frac{\mathrm{d}\mathbf{l} \times \mathbf{r}_k}{|\mathbf{r}_k|^3}}_{\hat{\mathbf{V}}_{ij}} \qquad x_5 = x_1 \tag{2.8}$$

with $\mathbf{r}_k$ being the vector pointing from the k-th vortex in the circle to the point P_j as shown in FIGURE 2.7.
In this way the total induced velocity at a point i is the sum of the induced velocities that the single vortex ring j impresses at the selected point:

$$\mathbf{V}_j = \sum_{j=1}^{m} \frac{\Gamma_j}{4\pi} \hat{\mathbf{V}}_{ij} \qquad i = 1, \ldots, m \tag{2.9}$$

Thus, (2.5a) becomes:

$$\mathbf{V}_\infty \cdot \mathbf{n}_i = -\left(\sum_{j=1}^{m} \frac{\Gamma_j}{4\pi} \hat{\mathbf{V}}_{ij}\right) \cdot \mathbf{n}_i \qquad i = 1, \ldots, m \tag{2.10}$$

This corresponds to a set of m linear equations, one for each panel, in the unknowns Γ_j that can be solved. VSPAERO uses an iterative approach to reduce the computational cost instead of directly trying to solve the system [6].
A final remark must be made on the Kutta condition at the trailing edge: since the wake is modelled as a group of ring vortices, it is necessary to set their intensity equal to the wings trailing edge, so that the Kutta condition can be enforced. This means that the circulation at the trailing edge is set to zero, hence also the differential pressure is zero (using the Bernoulli equation). In this way, the adjacent unbounded vortices cancel each other, leaving only the two external vortices that model the wake. A general scheme of this method is given in FIGURE 2.8.

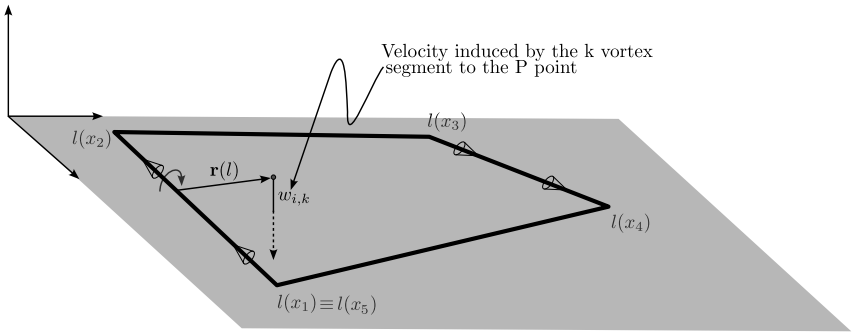

Figure 2.7: The velocity field induced by a ring vortex

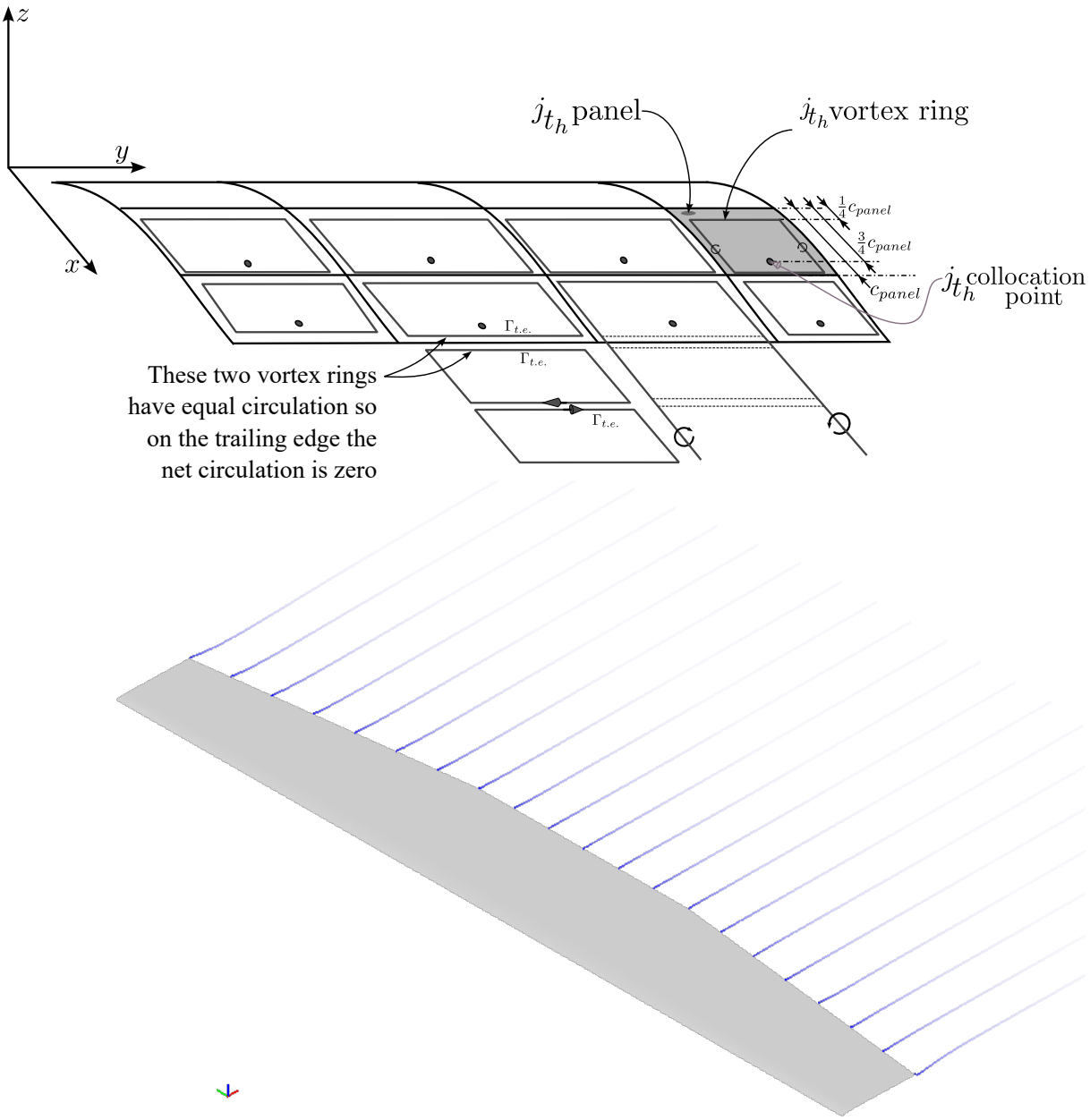

Figure 2.8: Scheme of the discretization used by VSPAERO and visualization of the results

2.4 Calculation of the Aerodynamic Centre Position of the Wing

2.4.1 Analysis the Isolated Wing

When the full configuration of the aircraft is analysed, it is customary to take the reference pole in the centre of gravity, while in this case it will be shown that taking the aerodynamic centre of the wing as a pole is more appropriate for showing the difference between wing and wing-body interaction on the aircraft stability. Because the coordinates of this special pole are not known, an arbitrary pole has been chosen as reported in the last column of TABLE A1.
To conduct the analysis the `.vsp3` file has to be loaded into OpenVSP, then all the parts not necessary for the wing analysis (e.g., the fuselage, tailplane, nacelles, ...) must be deleted. In some case it is necessary to modify the computational grid from the default exported by JPAD. This operation can be done using the appropriate menus as shown in FIGURE 2.9. Mach number was set to 0.001.

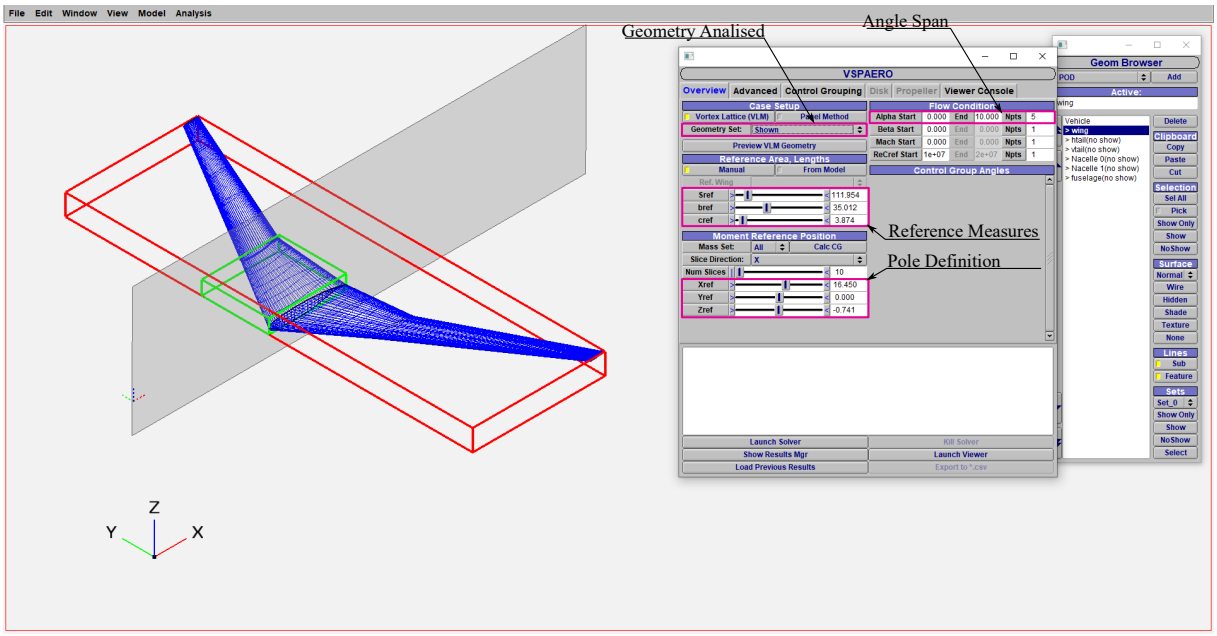

Figure 2.9: Options for running an analysis with VSPAERO

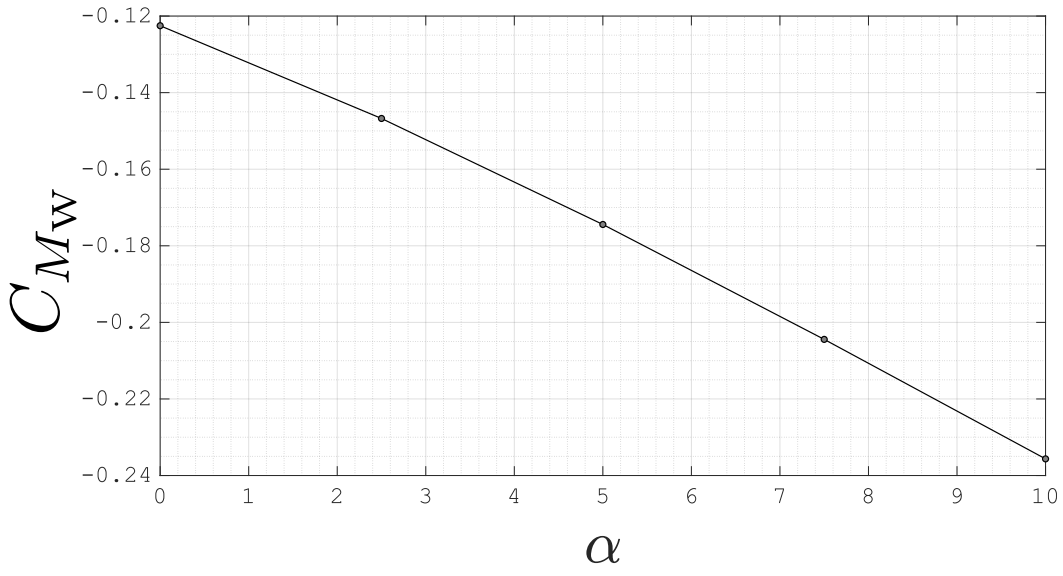

Figure 2.10: Results from VSPAERO for the wing of the A220-300

When the geometry has been set up, the model is ready to be analysed by VSPAERO. The interface is shown in FIGURE 2.9, highlighting the field where geometric data defined in TABLE 2.1 and TABLE A1 have to be inserted. Angle span has been set from 0 deg to 10 deg with a spacing of 2.5 deg so that the analysis falls into the linear trait of the forces/moments vs. angles relations as shown in FIGURE 2.10. Results for each airplane are listed in TABLE A3 with the obtained value of the coefficient (evaluated using the procedure explained at SECTION 2.5).

2.4.2 Evaluation of the Wing Aerodynamic Centre

The aim of this process is to obtain the values of various aerodynamic coefficients (e.g., the lift coefficient, the pitch moment coefficient, ...) for different configurations of wing and body.
Once the moment and lift coefficients of the isolated wing, taken about the arbitrary pole, have been evaluated with VSPAERO, the position of the aerodynamic centre can be calculated. To show the procedure to obtain this quantity, lets take an arbitrary pole, called A. Moment of the aerodynamic force around this pole will be given by the following relation (supposing that lift is applied in its reduction centre):

$$\mathbf{M}^{(A)} = (A - P_{\text{c.p.}}) \tag{2.11}$$

Let's now take another point, called B. Using (2.11) in this case we obtain:

$$\begin{aligned}\mathbf{M}^{(B)} =&(B - P_{c.p.}) \times \mathbf{L} = [(B - A) + (A - P_{\text{c.p.}})] \times \mathbf{L} \\ \mathbf{M}^{(B)} =&\mathbf{M}^{(A)} + (B - A) \times \mathbf{L}\end{aligned}$$

Making this equation dimensionless and taking the module it follows:

$$C_M^{(B)} = \frac{M^{(B)}}{\overline{q}_\infty S_{\text{ref}} \bar{c}} = C_M^{(A)} + (\overline{x}_b - \overline{x}_a) C_L \tag{2.12}$$

To find the aerodynamic centre of the wing, the invariance of C_M with respect to the angle of attack must be imposed:

$$C_M^{(B)} \equiv C_{M_{\text{a.c.(W)}}} \Leftrightarrow \frac{\partial C_M^{(B)}}{\partial \alpha} = \frac{\partial C_M^{(A)}}{\partial \alpha} + [\overline{x}_{\text{a.c.(W)}} - \overline{x}_a] \frac{\partial C_L}{\partial \alpha} = 0 \tag{2.13}$$

and the following relation is obtained:

$$\frac{C_{M_\alpha}}{C_{L_\alpha}} = [\overline{x}_{\text{a.c.(W)}} - \overline{x}_a] \tag{2.14}$$

Using values of C_M from the isolated wing with respect to the point at $0.25\bar{c}$, employing the procedure explained at SECTION 2.5, the required derivatives can be evaluated and so the relative position of the wing aerodynamic centre with respect to the point chosen. TABLE A3 contains all lift and pitching moment coefficients for the isolated wing, the value expressed by (2.14) and the coordinates of the wing aerodynamic centre.

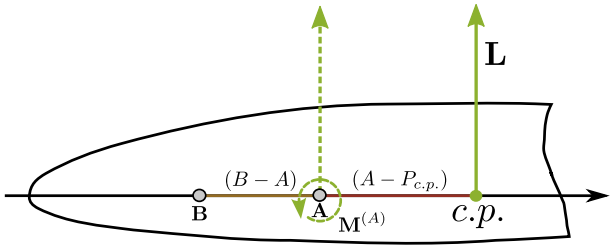

Figure 2.11: Relating the moment around pole B to the moment around pole A

For the vehicles marked with (∗) the C_{M_α} value is not correct because, for these wings, the reference point happens to be the aerodynamic centre of the wing. When the point is chosen to be the aerodynamic centre, C_M values obtained running a VSPAERO analysis will assume an irregular trend and they will change in magnitude very little with α compared to C_M values taken at other points. FIGURE 2.12 shows the behaviour of C_M when the pole is:

- ahead of the wing a.c.;
- at the wing a.c.;
- behind the wing a.c.

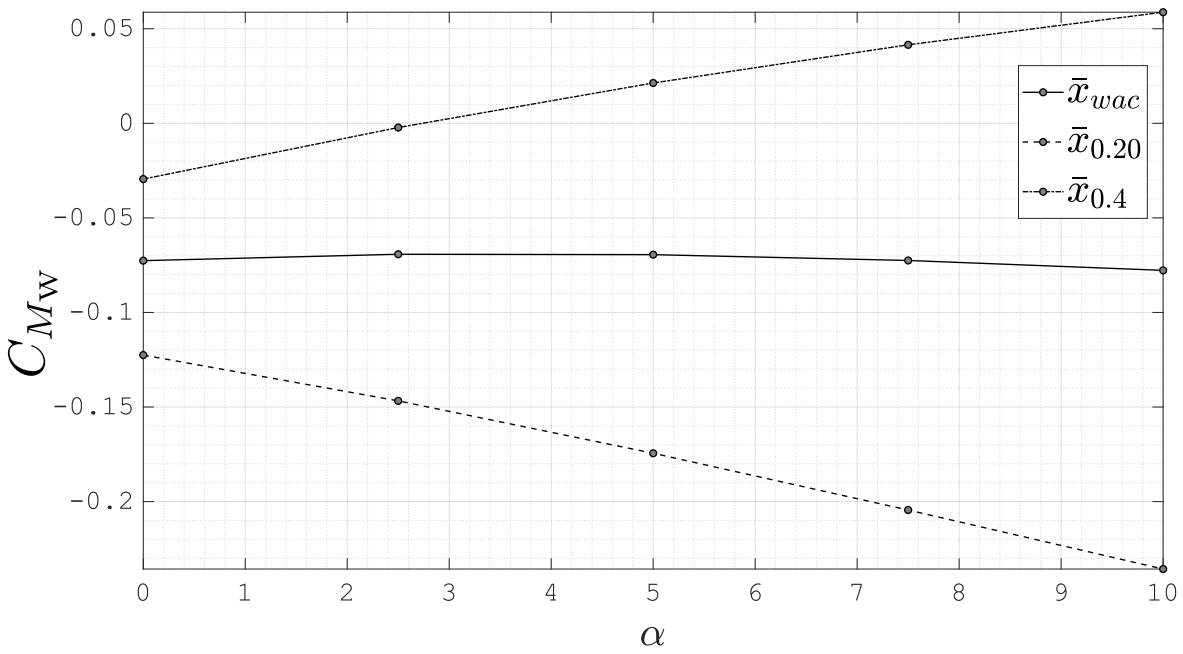

Figure 2.12: Comparison among the moments taken at three points for the A220-300

2.5 Evaluating the Aerodynamic Derivatives

The output of the VSPAERO simulation consists in several files, but only two are necessary for this analysis:

- a `Results.csv` file containing the results of the analysis, e.g., values of different coefficients with respect of the angle;
- a `DegenGeom.csv` file containing the point of the discretized geometry used to run the simulation.

The structure of the first file is shown in FIGURE 2.13. The values of the angles of attack and sideslip are set to span between 0 and 10 degrees. This interval corresponds to the linear trait of the C_M vs. C_L curves, therefore, the evaluation of the derivatives of such functions is reduced to compute the angular coefficient of the straight lines. MATLAB is used to obtain these values importing the data stored in the `.csv` files into matrices and fitting them using the standard MATLAB function `polyfit`. All the results shown in TABLES A4 to A5 are obtained using this procedure.

294	CFz	0	0	0	0	0
295	CL	0	0	0	0	0
296	CMl	-0.000000195012	0.000248219074	0.000494750629	0.000737531269	0.000974660866
297	CMm	-0.02399190364	-0.02424700066	-0.02502178262	-0.02630650165	-0.02809380448
298	CMn	-0.0000004454	-0.00571134467	-0.01137889405	-0.01695916678	-0.02241078773
299	CMx	0.000000195012	-0.00024821907	-0.00049475063	-0.00073753127	-0.00097466087
300	CMy	-0.02399190364	-0.02424700066	-0.02502178262	-0.02630650165	-0.02809380448
301	CMz	0.0000004454	0.00571134467	0.011378894053	0.01695916678	0.022410787734
302	CS	0	0	0	0	0
303	E	0	0	0	0	0
304	Fopt	0	0	0	0	0
305	L_D	0	0	0	0	0
306	Mach	0	0	0	0	0
307	Re_1e6	10	10	10	10	10

Figure 2.13: Example of the results file

2.5.1 Wing

Wing moment coefficients are evaluated using as reference pole the centre at a quarter chord instead of the aerodynamic centre. The quantities reported in TABLE A4 are:

- the lift coefficient $C_{L_{\alpha,\mathrm{W}}}$ for the isolated wing;

- the pitching moment $C_{M_{\alpha,\mathrm{W}}}$;
- the roll moment $C_{\mathcal{L}_{\beta,\mathrm{W}}}$;
- the yaw moment $C_{\mathcal{N}_{\beta,\mathrm{W}}}$

The second coefficient is tied to longitudinal stability, while the last two are instead linked to the latero-directional stability. It is useful to remember that these coefficients are expressed in the BRF and not in the CRF. This means that:

- a positive $C_{M_{\alpha,\mathrm{W}}}$ corresponds to an unstable longitudinal behaviour at the given component, because, for a variation of α from the equilibrium position, the system responds moving away from the such position;
- a positive $C_{\mathcal{L}_{\beta,\mathrm{W}}}$ also corresponds to an unstable lateral behaviour because, for a variation of sideslip angle β, the vehicle will tend to move into a spiral;
- a positive $C_{\mathcal{N}_{\beta,\mathrm{W}}}$ coefficient corresponds to a stable directional behaviour since in this case the system tends to reduce the perturbation, i.e., the component tends to move towards the direction of the current.

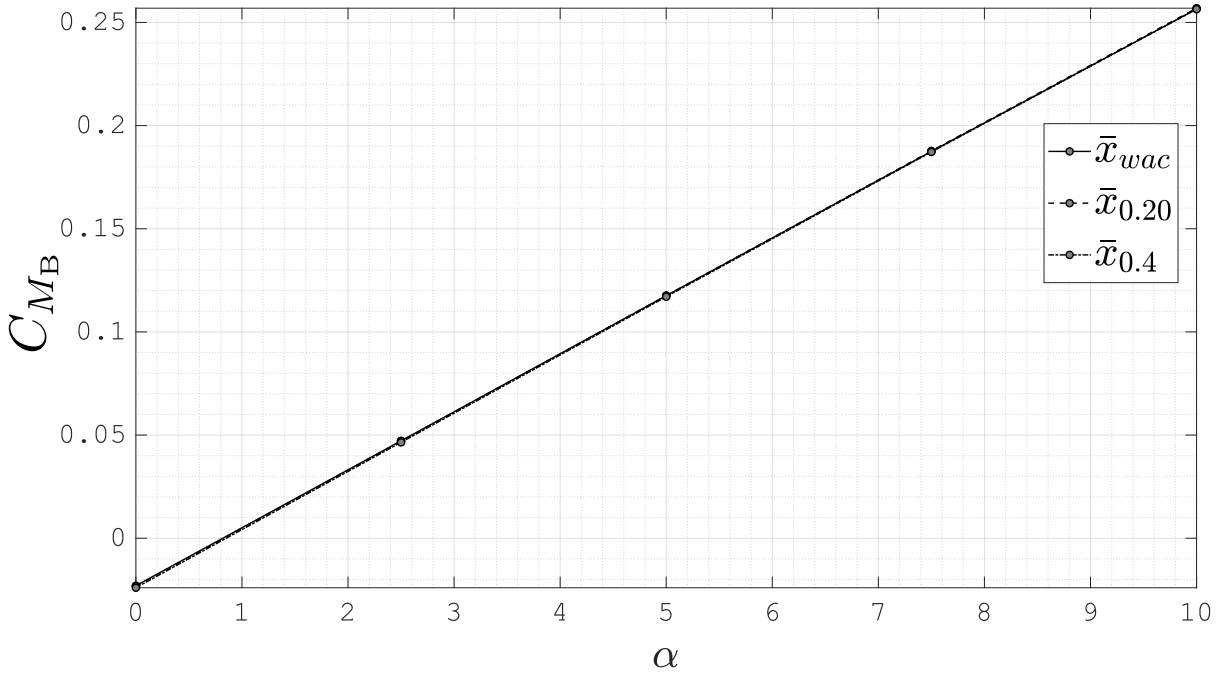

Figure 2.14: Differences among $C_{M_{\mathrm{B}}}$ values for an ATR-42 evaluated at three different points

Generally it would be expected for a wing to have a negative $C_{M_{\alpha,\mathrm{W}}}$ and a positive $C_{\mathcal{N}_{\beta,\mathrm{W}}}$ coefficient. It is more difficult to make a general argument for the rolling coefficient because it depends both on the wing itself (through its angle of bank and sweep angle) and how it is installed on the fuselage.
Some tweaks had to be made to different wing computational grids, since some numerical solutions were not physical. One of the most critical cases was the G400 whose results are reported in FIGURES 2.15 and 2.16. To obtain better results it was necessary to refine the spanwise grid distribution towards the wingtip.

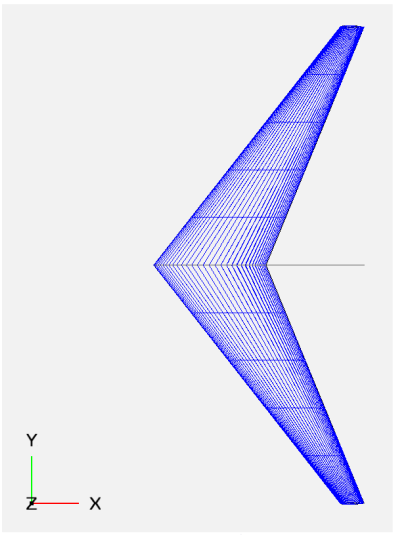

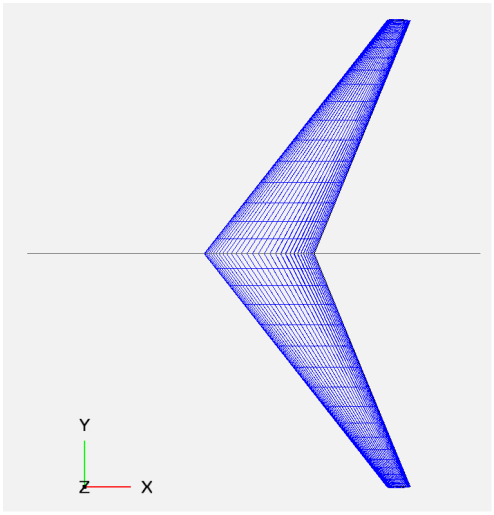

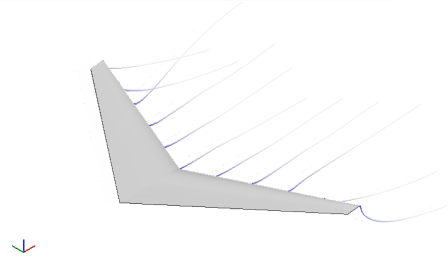

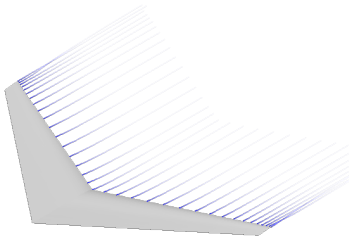

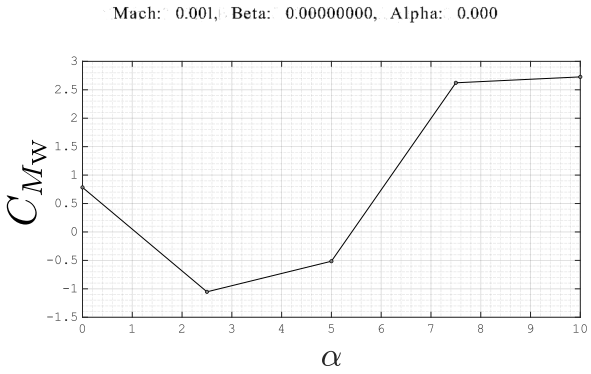

Figure 2.15: Results for the pitching moment of a G400 with the default grid from JPAD

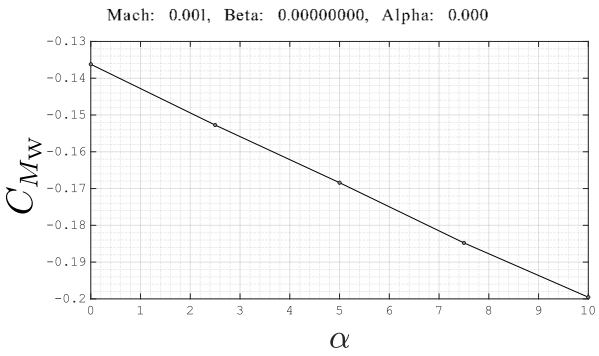

Figure 2.16: The same results for the G400 with a finer grid

2.5.2 Isolated Fuselage

The fuselage is a non-lifting body, therefore it is known that its forces system is equivalent to a free couple, whose effect is to reduce aircraft stability. This behaviour is also shown by VSPAERO because, if the pole has changed, the $C_{M_{\alpha,B}}$:

- remains positive;
- does not vary with the pole as FIGURE 2.14 shows for the ATR-42 fuselage.

As expected, VSPAERO did not provide a significant value for the lift coefficient.
A similar result is obtained analysing the latero-directional stability. As matter of fact, it is shown in FIGURE 2.17 how the results of the yawing coefficients do not change when the pole's position varies.
Results for the isolated fuselage are reported in TABLE A6.

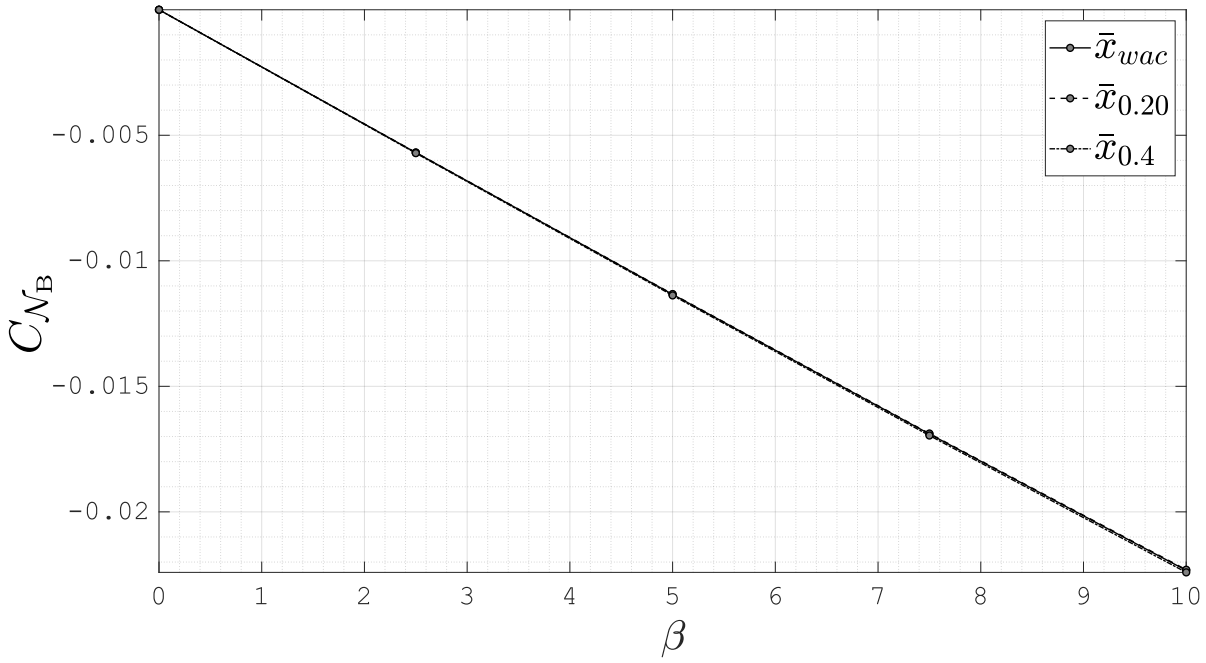

Figure 2.17: Differences among $C_{\mathcal{N}_B}$ values for an ATR-42 evaluated at three different points

2.5.3 Wing and Body

To conduct the analysis for the wing and body configuration, the aerodynamic centre of the wing is chosen as the reference pole for the moments. The setup for the analysis is the same seen in the previous cases and its geometry can be seen in FIGURE 2.18. Longitudinal and latero-directional coefficients are listed in TABLE A5.

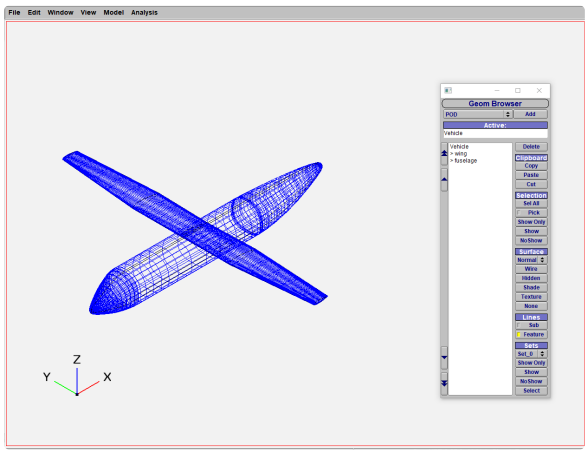

Figure 2.18: Visualization of the grid for a wing-body configuration of an ATR-42

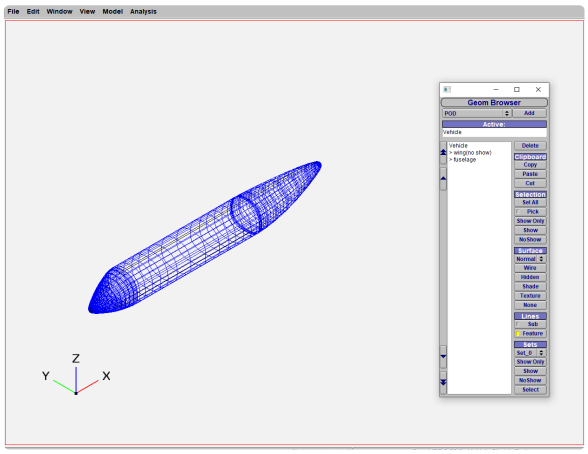

Figure 2.19: Visualization of the grid for a fuselage of an ATR-42

2.6 Discussion of Results

It is here anticipated that most of the wings have negative pitching moment coefficients and negative pitching moment derivatives, meaning that they all tend to pitch down and exhibit a stable behaviour at pitching with the chosen reference point. For the yawing behaviour, there is no clear trend as, out of 27 wings analysed, almost half resulted in a positive yawing moment (stable), while the other half resulted in a negative yawing derivative.

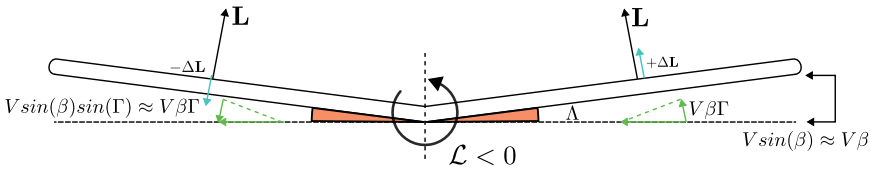

Figure 2.20: Effects of the Dihedral angle with respect to rolling

It is noted that for single or multi-cranked wings, the sweep angle had to be superior to 30 degrees to achieve stability at yawing, but almost all rectangular tapered wings (excepted for the Q400 wing) presented instead stable behaviour. The sweep angle can generally increase stability at yawing because it makes the windward half-wing to generate an increase of lift and drag as shown in FIGURE 2.21. This unbalanced system of forces has the effect to rotate the airplane towards the wind direction. This phenomenon could explain the directional stability among airplanes with rather large values of sweep angle. The increase of lift experienced by the upwind semi-wing is also shown by VSPAERO analysis and reported in FIGURE 2.21.

For the body and wing configuration there is no ambiguity on the behaviour of the system, given that the instability of the fuselage overcomes the stabilizing effect (when present) of the isolated wing, hence all of the 27 wing-body configurations presents an unstable behaviour.

Considering roll stability, it results that all wings except three are stable to roll because of the lift increment on the downwind half-wings due to sweep and dihedral angles. This increase of lift generates an unbalanced force that causes a negative rolling moment for positive angles of sideslip. The aforementioned effects can be visualised in FIGURES 2.20 and 2.7. The only three cases of positive (unstable) $C_{\mathcal{L}_{\beta,\mathrm{B}}}$ is experienced in aircraft whose wings have neither a dihedral angle nor a sweep angle (Canadair CL-415 and C-130H), while the last one (AN-32) has a negative dihedral angle. For the first two cases, though, the wing-body configuration is stable to roll, because of the interference of the fuselage on the wing aerodynamic system, being both high-wing aircraft. Conversely, the wing of the AN-32 remains laterally unstable. In general, it is observed that all high-wing airplanes present a lower $C_{\mathcal{L}_{\beta,\mathrm{B}}}$ of the isolated wing (being more negative) that the one of wing-body configuration. The opposite is true for low-wing airplanes. Reference [7] gives a brief explanation of this phenomenon as it is linked to the variation of angle of attack that the cross field causes in the vicinity of the fuselage.

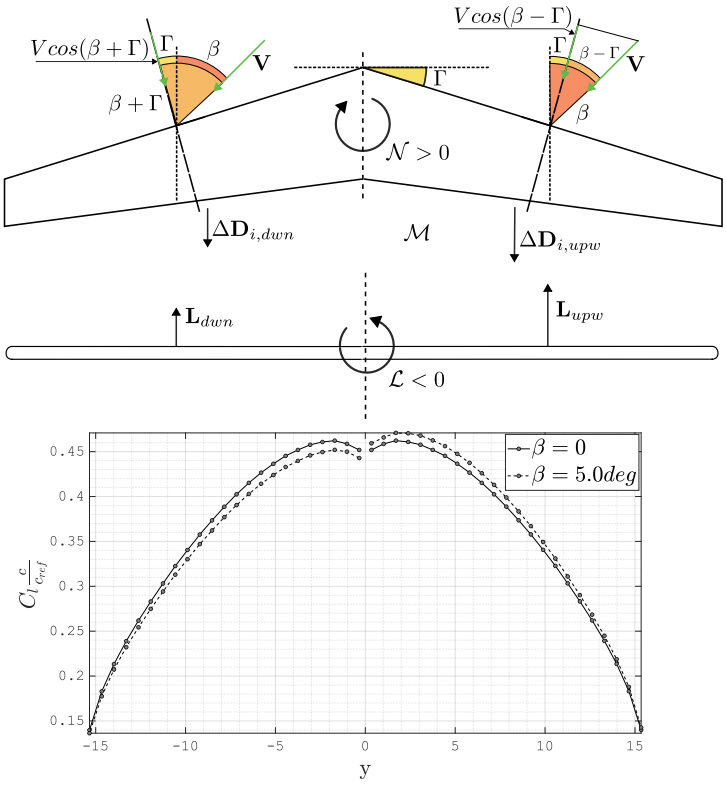

Figure 2.21: Effects on yawing and rolling associated with a sweep angle

Lastly, the pitching behaviour of the wing-body system is unstable, i.e., the moment coefficient slope is positive since there is no horizontal tail to stabilize the configuration.

Chapter 3

Semi-Empirical Methods and Results Comparison

Two semi-empirical methods were used to validate some of the results obtained from the lattice vortex analysis, namely the Munk strip method, useful to predict pitching and yawing moment coefficients of the isolated body, and the Multhopp method (later included into the DATCOM database), used to predict the behaviour of the fuselage when combined with the wing. Both the vortex lattice method and these two semi-empirical methods rely on the same hypothesis on the nature of flow field.

3.1 Munk Theory for Isolated Body Derivatives

Since the hypotheses for the slender bodies are the same as the ones expressed in Section 2.3 about the VLM, all the considerations about the velocity can be made. This means that the velocity potential Φ can be introduced and it has to satisfy the same equation (2.4) and BCs (2.5), as defined in Section 2.3. A body like a fuselage displaces the fluid around it when moving. To make it move, it is necessary to overcome the inertia of the body itself and the fluid. Considering the fluid and the fuselage as a system, the total kinetic energy is given by the sum of the two kinetic energies [8]:

$$\mathcal{T}_{\text{total}} = \frac{1}{2} M_B V^2 + \frac{1}{2} M_a V^2 \tag{3.1}$$

where the term M_a is the apparent mass factor of the body and is defined as:

$$M_a \equiv \frac{\mathcal{T}_{\text{fluid}}}{\frac{1}{2}V^2} = K\rho_\infty \tag{3.2}$$

so that the second term in the expression of $\mathcal{T}_{\text{total}}$ can be expressed as:

$$\frac{1}{2} M_a V^2 = \frac{1}{2} \frac{\mathcal{T}_{\text{fluid}}}{\frac{1}{2}V^2} V^2 = \mathcal{T}_{\text{fluid}} \tag{3.3}$$

It is now useful to introduce the concept of impulsive force. The motion of a body in a fluid that satisfies the above-cited hypothesis can be modelled as a series of impulsive forces applied sequentially. A force, to be defined impulsive, has to change by a finite amount the velocity and momentum in a very short period of time. The relation between change in momentum and force is [9]:

$$\mathbf{q}(t_0 + \Delta t) - \mathbf{q}(t_0) = \int_{t_0}^{t_0+\Delta t} \mathbf{F} \mathrm{d}t \equiv \mathcal{I} \tag{3.4}$$

where the integral is defined as the impulse. Now, taking a particle of fluid, the variation of its momentum due to impulsive forces can be expressed (using the balance of momentum in the Lagrangian form for the small control mass) as:

$$m\left[\mathbf{V}(t_1) - \mathbf{V}(t_0)\right] = \int_{t_0}^{t_0+\Delta t} \mathbf{F} \mathrm{d}t = -\int_{t_0}^{t_0+\Delta t} \nabla \left(\frac{p}{\rho}\right) \mathrm{d}t \tag{3.5}$$

since on an element of fluid only acts pressure as the viscous effects have been neglected. The last term of the equation is the impulsive pressure and can be related to velocity potential as:

$$\mathbf{V}(t) = \nabla\Phi = -\int_{t0}^{t0+\Delta t} \nabla\left(\frac{p}{\rho}\right) \mathrm{d}t = -\frac{1}{\rho}\nabla P_I$$
$$\nabla(\Phi + \frac{P_I}{\rho}) = 0 \rightarrow -\Phi\rho = P_I$$

The work done by this impulsive pressure on the fluid is given by the difference of kinetic energy. If the fluid is moved from rest, then $\Delta\mathcal{T} = \mathcal{T} - 0$:

$$\mathcal{T} = \int_S \underbrace{-\rho\Phi}_{P_I} \underbrace{\left(\frac{0 + \frac{\partial\Phi}{\partial n}}{2}\right)}_{\text{time-averaged velocity}} \mathrm{d}S \tag{3.6}$$

If a body is moving in an inviscid fluid, there is no drag and no lift, but this does not mean that also the moment is null. In fact, considering a body moving on a straight line with constant velocity and assuming that there is a component of momentum of the flow perpendicular to the velocity $\mathbf{V}$ with value [3, 9]:

$$q = K\rho_\infty V_\infty \tag{3.7}$$

Fixing a point in the plane containing the momentum vector, an angular momentum is generated from this momentum component perpendicular to the velocity direction. By the Euler's second law, the time derivative of the angular momentum equals the applied moment. The magnitude of this moment is the magnitude of the cross product of the velocity and momentum vectors:

$$M = |\mathbf{V} \times \mathbf{q}| = V(K\rho_\infty V_\infty) \tag{3.8}$$

This means that an equal and opposite moment must be applied to the body to reach an equilibrium. Conversely, if the body does not experience any moment, the momentum of the flow must be entirely in the line of motion of the body.
Consider a body that is in equilibrium in a constant flow. If the body is slightly turned by a small angle $\mathrm{d}\alpha$, the direction of the body velocity will be no longer parallel to the momentum of the flow, hence a moment is generated. If the moment tends to reduce the disturbance — meaning that for a clockwise rotation, the moment is counterclockwise and vice-versa — the equilibrium is said to be stable. In this case, to turn the body, work must be done on the fluid, since the fluid tends to oppose this rotation, and its kinetic energy increases by an amount given by $\mathrm{d}\mathcal{T}' = M\mathrm{d}\alpha$. In this case $\mathrm{d}\alpha$ and M have opposite sign (M opposes the disturbance). Thus, using the same sign convention for both gives $\mathrm{d}\mathcal{T} = -\mathrm{d}\mathcal{T}' = M\mathrm{d}\alpha$. As a result, if the body lies in a orientation for which $\mathcal{T}$ is maximum, a perturbation from this position will reduce the kinetic energy, hence the sign of the derivative will be negative and the moment will be opposite to the angular displacement, meaning that the equilibrium is stable. Summarising:

$$\frac{\mathrm{d}\mathcal{T}}{\mathrm{d}\alpha} > 0 \qquad \text{stable}$$
$$\frac{\mathrm{d}\mathcal{T}}{\mathrm{d}\alpha} < 0 \qquad \text{unstable}$$

The kinetic energy is then different for directions of motion other than specified ones, but it is always a positive number. Therefore, as the orientation of the motion of the body is changed from a fixed orientation to the opposite, there must be two directions for $\mathbf{V}$ somewhere between, for which the kinetic energy is maximum and minimum. In these two directions the body is in equilibrium.
Supposing now that the body lies in one of these directions, called $\tilde{x}_1$, it will have a momentum parallel to the direction of the motion defined again as (3.7):

$$q = K\rho_\infty V_\infty \tag{3.7}$$

Maintaining the body oriented along this direction, let us move the fluid along an axis perpendicular to this one, named $\tilde{x}_2$. In a general case $\tilde{x}_2$ could be a non-equilibrium axis, hence there could be momentum

components along all three axes, then:

$$q_1 = D\rho_\infty V_\infty \qquad \tilde{x}_1 \tag{3.9a}$$
$$q_2 = C\rho_\infty V_\infty \qquad \tilde{x}_2 \tag{3.9b}$$
$$q_3 = E\rho_\infty V_\infty \qquad \tilde{x}_3 \tag{3.9c}$$

where $\tilde{x}_3$ is a direction perpendicular to the first two. Taking now a generic line of motion between $\tilde{x}_1$ and $\tilde{x}_2$, forming an angle of α with $\tilde{x}_1$, there will be a momentum:

$$q_1 = K\rho_\infty V_\infty \cos\alpha + D\rho_\infty V_\infty \sin\alpha \tag{3.10a}$$
$$q_2 = C\rho_\infty V_\infty \sin\alpha \tag{3.10b}$$

while the velocity will be:

$$V_1 = V_\infty \cos\alpha \tag{3.11a}$$
$$V_2 = V_\infty \sin\alpha \tag{3.11b}$$

Subsequently, the kinetic energy will be:

$$\begin{aligned}\mathcal{T} =& \frac{1}{2}\mathbf{q}\cdot\mathbf{V}_\infty = \\ &= \frac{\rho_\infty}{2}V_\infty^2[K_1\cos^2\alpha + D\sin\alpha\cos\alpha + C\sin^2\alpha] \\ M =& \frac{\mathrm{d}\mathcal{T}}{\mathrm{d}\alpha} = \frac{\rho_\infty}{2}V_\infty^2[(C-K_1)\sin(2\alpha) + D\cos(2\alpha)]\end{aligned}$$

For $\alpha = 0$ the direction coincides with the direction of equilibrium, hence it must be $M = 0$:

$$M = \left.\frac{\mathrm{d}\mathcal{T}}{\mathrm{d}\alpha}\right|_{\alpha=0} = \frac{\rho_\infty}{2}V_\infty^2[(C-K_1)\sin(2\alpha) + D\cos(2\alpha)]_{\alpha=0} = 0 \rightarrow D = 0$$

From this condition, it follows that the apparent mass coefficient D must be zero. The moment becomes:

$$M = \frac{\mathrm{d}\mathcal{T}}{\mathrm{d}\alpha} = \frac{\rho_\infty}{2}V_\infty^2(C-K_1)\sin(2\alpha) \tag{3.12}$$

This means that if the body is moving in direction $\tilde{x}_2$ there will not be any momentum component along $\tilde{x}_1$, since it is a direction of equilibrium.
Taking this result into account, it is possible to obtain other two directions that are equilibrium axes (cf. Ref. [9] for the explanation of the phenomenon in a more rigorous way). If these three axes are taken as a reference system, the momentum along a generic axis in the $\tilde{x}_1$–$\tilde{x}_2$ plane will be given by:

$$q_1 = K_1\rho_\infty V_\infty \cos\alpha \tag{3.13a}$$
$$q_2 = K_2\rho_\infty V_\infty \sin\alpha \tag{3.13b}$$

Using Euler's law for the momentum, applied in the BRF, gives:

$$\frac{\mathrm{d}\mathbf{K}}{\mathrm{d}t} = -\mathbf{V}_\mathrm{B}\times\mathbf{q} + \mathbf{M}^{(\mathrm{F})} \tag{3.14}$$

where $\mathbf{M}^{(\mathrm{F})}$ is the moment acting on the fluid, $\mathbf{K}$ is the angular momentum of the fluid. If the motion is stationary, the previous formula becomes:

$$\mathbf{M}^{(\mathrm{F})} = \mathbf{V}_\mathrm{B}\times\mathbf{q} \tag{3.15}$$

To obtain the moment the fluid F exerts on the body B, using Newton's laws of motion:

$$\mathbf{M}^{(\mathrm{B})} = -\mathbf{M}^{(\mathrm{F})}$$
$$\mathbf{M}^{(\mathrm{B})} = -\mathbf{V}_\mathrm{B}\times\mathbf{q}$$

Considering a flow at an angle of attack, carrying out the cross product:

$$\mathbf{M}^{(\mathrm{B})} = V_\infty^2\rho_\infty \begin{vmatrix} \mathbf{i} & \mathbf{j} & \mathbf{k} \\ K_1\cos\alpha & 0 & K_2\sin\alpha \\ \cos\alpha & 0 & \sin\alpha \end{vmatrix} = \rho_\infty(K_2-K_1)V_\infty^2\sin\alpha\cos\alpha\mathbf{j} = \frac{1}{2}\rho_\infty(K_2-K_1)V_\infty^2\sin(2\alpha)\mathbf{j} \tag{3.16}$$

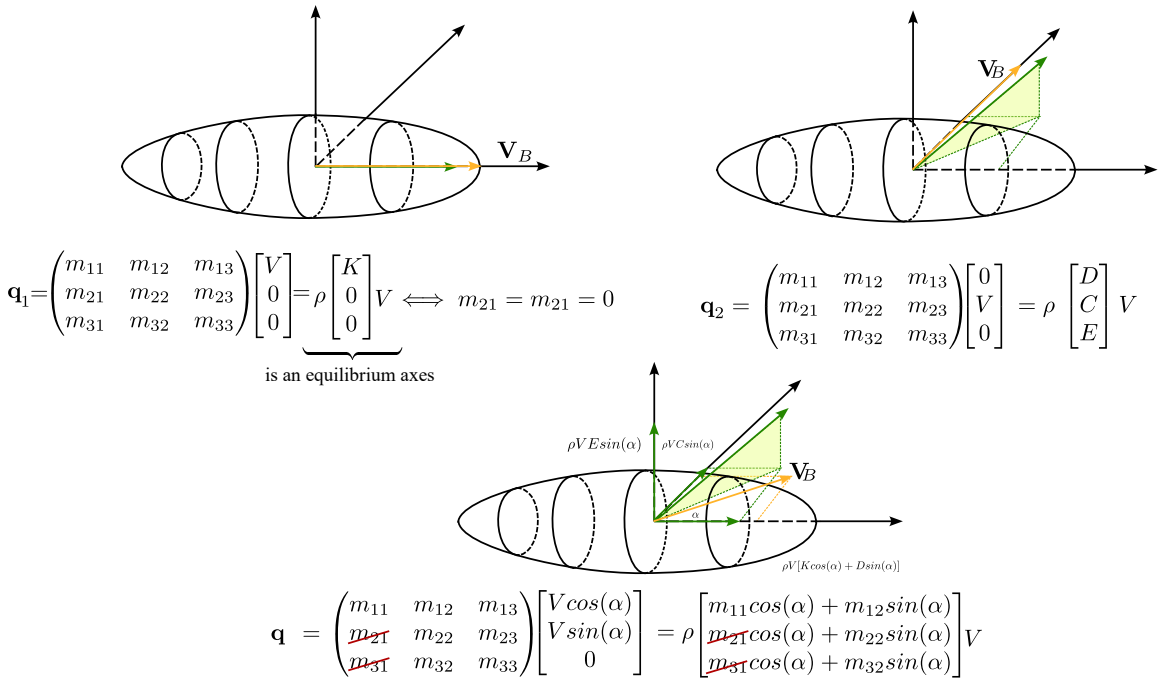

Figure 3.1: Momentum orientation in the three cases described (for a detailed explanation of the matrix see Reference [9])

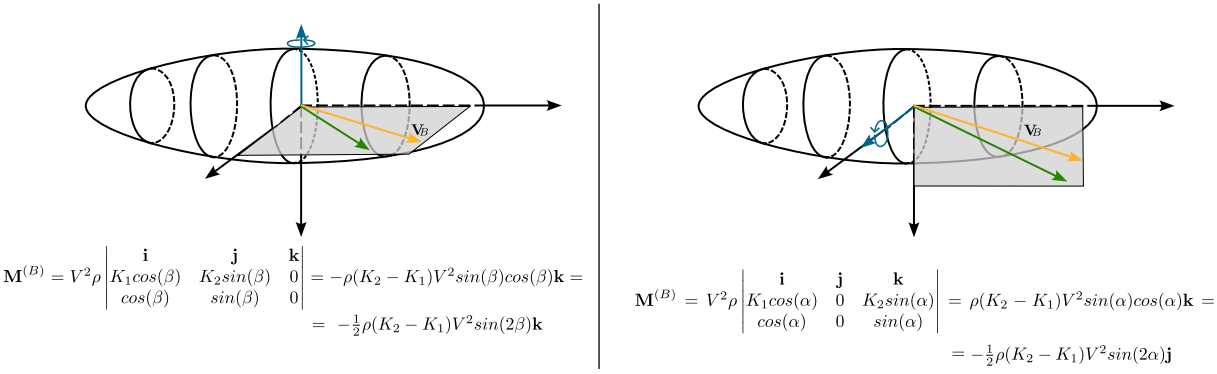

Figure 3.2: Moment orientation for a current with angle of attack and sideslip

FIGURE 3.2 clarifies the meaning of the sign of the moment both for a flow with an angle of attack and for a flow with an angle of sideslip. If $K_2 > K_1$ this moment tends to increase the value of α, hence it is unstable.The apparent mass coefficients can be expressed in term of the body volume $\mathcal{V}$, as

$$K_i = k_i \mathcal{V}$$

and for small angles of attack, where $\sin(2\alpha) \approx 2\alpha$, equation (3.16) becomes:

$$M_y = (k_2 - k_1) \rho_\infty V_\infty^2 \alpha \mathcal{V} \tag{3.17}$$

These results are extended to non axisymmetric bodies subdividing their planforms into stripes of length Δx considered to be axisymmetric obtaining:

$$C_{M_{\alpha,\mathrm{B}}} = \frac{(k_2 - k_1)\pi}{S_\mathrm{W} \bar{c}} \int_0^{l_\mathrm{B}} b(x)^2 \, \mathrm{d}x \tag{3.18a}$$

$$C_{\mathcal{N}_{\beta,\mathrm{B}}} = \frac{(k_2 - k_1)\pi}{S_\mathrm{W} b_\mathrm{W}} \int_0^{l_\mathrm{B}} h(x)^2 \, \mathrm{d}x \tag{3.18b}$$

where $b(x)$ is the width of the fuselage section at a given station x along the longitudinal axis, $h(x)$ is the height along the z-axis, l_B is the total length of the fuselage. Wing span S_W, mean aerodynamic chord $\bar{c}$,

and wing span b_W are chosen as reference parameters for making the moment non-dimensional. Starting from these relations, a MATLAB code has been developed to evaluate the required derivatives.
The geometrical data required to evaluate the volume of the stripes are stored into the `Degen_Geom.csv`, created by VSPAERO after an analysis has been run, as a set of (x, y, z) coordinates. MATLAB code reads all the triplets of point coordinates and uses the information to build a discretized version of the airplane (using the same discretization employed by VSPAERO) and evaluates the length, width, and height of the stripes. Then it evaluates strip-by-strip the summation:

$$C_{M_{\alpha,B}} = \frac{(k_2 - k_1)\pi}{S_W \bar{c}} \sum_{i=1}^{n} b_i^2 \Delta x_i \tag{3.19a}$$

$$C_{N_{\beta,B}} = \frac{(k_2 - k_1)\pi}{S_W b_W} \sum_{i=1}^{n} h_i^2 \Delta x_i \tag{3.19b}$$

In this case $h(x)$ and $b(x)$ have been replaced with respectively the width and height of the i-th fuselage strip. The structure pf the MATLAB code employed to obtain the values of these derivatives is reported in FIGURE 3.6. The term $k_2 - k_1$ is tabulated in relation with the fuselage slenderness ratio and it is plotted in FIGURE 3.5. The results are tabulated and compared with the ones obtained by VSPAERO.

3.2 Multhopp Method for Body with Wing Effects

The presence of a wing alters the flow field around the fuselage significantly, and as a consequence its behaviour. Reference [1] suggests that lifting forces that the body takes due to the wing are approximately of the same magnitude of the ones that the section of the wing substituted by the fuselage would take. A reference plane is chosen at an arbitrary distance x from the fuselage nose, so that it is perpendicular to the stream direction of the airplane. The lift of the rear part of the fuselage is obtained through momentum considerations. The phenomenon is stationary, so the integral of pressures on the fuselage surface ahead of the reference plane is equal to the change in vertical momentum passing through such plane. If the body is slender, the flow around a section of the fuselage can be considered bi-dimensional. Reference [4] shows that the vertical flow passing across a 2-D cylinder of diameter b is given by:

$$\dot{m} = \rho V_n \pi \left(\frac{b}{2}\right)^2 \tag{3.20}$$

where V_n is the velocity normal to the cylinder section.
For a fuselage, V_n is the component of $\mathbf{V}$ projected in a plane at right angles to the body axes and it is given by $V_n = V \sin\gamma$, with γ being the angle the current makes with the fuselage axis. This angle can be seen as the summation of the angle of attack of the body, plus the additional deviation angle induced by the wing circulation: $\gamma = \alpha + \epsilon$, with $\epsilon = \epsilon(x)$ as it varies along the fuselage.
Recalling (3.20), the rate of change of momentum is then given by:

$$L_{\text{aft}} = \dot{m} V_\infty \approx \rho_\infty V_\infty^2 \gamma(x)\, \pi \left(\frac{b}{2}\right)^2 \tag{3.21}$$

Differentiating (3.21), the rate of change of lift along the body axis is:

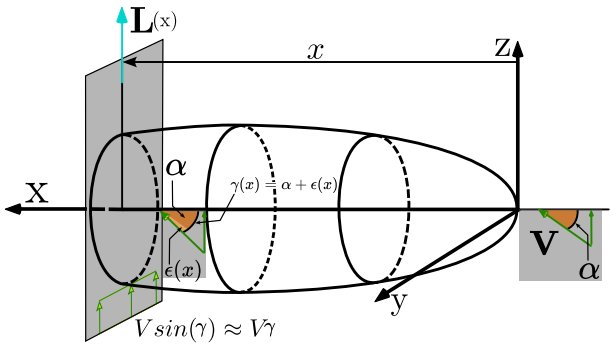

Figure 3.3: Definition of the arbitrary plane along the x-axis

$$\frac{\mathrm{d}L_{\text{aft}}}{\mathrm{d}x} = \frac{1}{2}\rho_\infty V_\infty^2 \frac{\mathrm{d}}{\mathrm{d}x}\left[\gamma(x) b^2(x)\right]$$

The moment can be obtained from a reference pole as the integral of the elemental lift $\mathrm{d}L$, acting on a segment $\mathrm{d}x$, multiplied by the distance of such segment to the pole reference:

$$M = -\int_0^{l_B} x \mathrm{d}L = -\int_0^{l_B} x \frac{\mathrm{d}L}{\mathrm{d}x}\,\mathrm{d}x =$$
$$= -\frac{1}{2}\rho_\infty V_\infty^2 \frac{\pi}{2} \int_0^{l_B} x \frac{\mathrm{d}}{\mathrm{d}x}\left[\gamma(x) b^2(x)\right]\mathrm{d}x$$

Integrating by parts and remembering that $b(x=0) = b(x=l_B) = 0$:

$$\begin{aligned} M =& -\frac{1}{2}\rho_\infty V_\infty^2 \frac{\pi}{2}\left(x\gamma(x)b^2(x)\Big|_0^{l_B} - \int_0^{l_B}\gamma(x)b^2(x)\,\mathrm{d}x\right) = \\ =& \frac{1}{2}\rho_\infty V_\infty^2 \frac{\pi}{2}\int_0^{l_B}\gamma(x)b^2(x)\,\mathrm{d}x \end{aligned} \tag{3.22}$$

The function describing the local angle the current makes with the fuselage axis (which is the contribution of wing circulation) has to be found. Since the stability is here investigated, the moment given by (3.22) has to be differentiated by the angle of attack:

$$\begin{aligned} \frac{\partial M}{\partial\alpha} =& \frac{1}{2}\rho_\infty V_\infty^2 \frac{\pi}{2}\int_0^{l_B}\frac{\partial\gamma(x)}{\partial\alpha}b^2(x)\,\mathrm{d}x = \frac{1}{2}\rho_\infty V_\infty^2 \frac{\pi}{2}\int_0^{l_B}\frac{\partial[\alpha+\epsilon(x)]}{\partial\alpha}b^2(x)\,\mathrm{d}x = \\ =& \frac{1}{2}\rho_\infty V_\infty^2 \frac{\pi}{2}\int_0^{l_B}\left(1+\frac{\partial\epsilon(x)}{\partial\alpha}\right)b^2(x)\,\mathrm{d}x \end{aligned} \tag{3.23}$$

The value of the derivative $\dfrac{\partial\epsilon(x)}{\partial\alpha}$ assumes different behaviours in relation to the position of the section with respect to the wing:

- ahead of the wing trailing edge, there is an upwash caused by the circulation of the wing and it reaches a peak in the proximity of the leading edge. The value of the derivative is tabulated in FIGURE 3.4 computed for a wing of aspect ratio $\mathit{AR} = 8$ and $C_{L_\alpha} = 4.5\ \mathrm{rad}^{-1}$. Reference [1] states that for other wings this value can be approximated scaling it by the effective wing C_{L_α};
- on the wing the current is practically parallel to the wing chord, hence the derivative is null;
- from the trailing edge going to the end of the fuselage, the current is deviated by the wing downwash, which can be considered as linearly varying from the wing trailing edge to the horizontal tail.

The integral for obtaining the pitching moment coefficients needs to be divided in two sections, one ahead of the wing, the other aft the wing, since the value of $\mathrm{d}\epsilon/\,\mathrm{d}\alpha$ is different. This means that, with varying angle of attack, the moment of the fuselage is no longer constant. It follows that the moment of the wing and body configuration about the aerodynamic centre of the isolated wing is no longer constant with α meaning that the aerodynamic centre of this configuration does not coincide with the one of the isolated wing.
A new MATLAB code had to be implemented using the same data contained in the `Degen_Geom.csv`, but it also required other geometrical data obtained from JPAD, like the position in the body reference frame of the horizontal tail apex (not included into the `Degen_Geom.csv`, since it was ignored in the analysis) and the position of the point at a quarter chord. The structure of this MATLAB code is represented in FIGURE 3.7. All these quantities were grouped in a `.csv` file that was passed as an input to the MATLAB code. They are required to evaluate the upwash and downwash gradients that the wing forms respectively ahead and behind the fuselage and that modify the behaviour of the fuselage itself. The additional data are listed in TABLE A8.
The upwash gradient is obtained from FIGURE 3.4, where it is plotted against the non-dimensional coordinates $\bar{x}_1$, $\bar{x}_2$, that identify the position of the i-th strip from a system of reference, whose origin is placed on the leading edge of the exposed root chord. The downwash gradient is estimated using a method provided by DATCOM and it is supposed to increase linearly from the exposed root chord trailing edge to the horizontal tail.

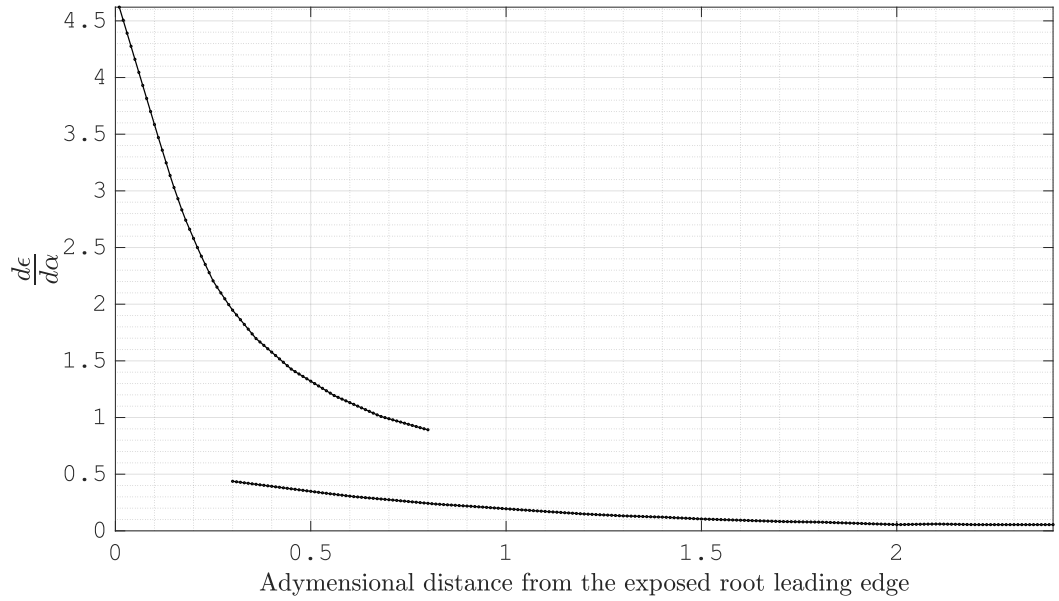

Figure 3.4: Value for the wing upwash gradient evaluated for a wing of $\mathit{AR} = 8$ and $C_{L_\alpha} = 4.5$ rad^{-1} [1]

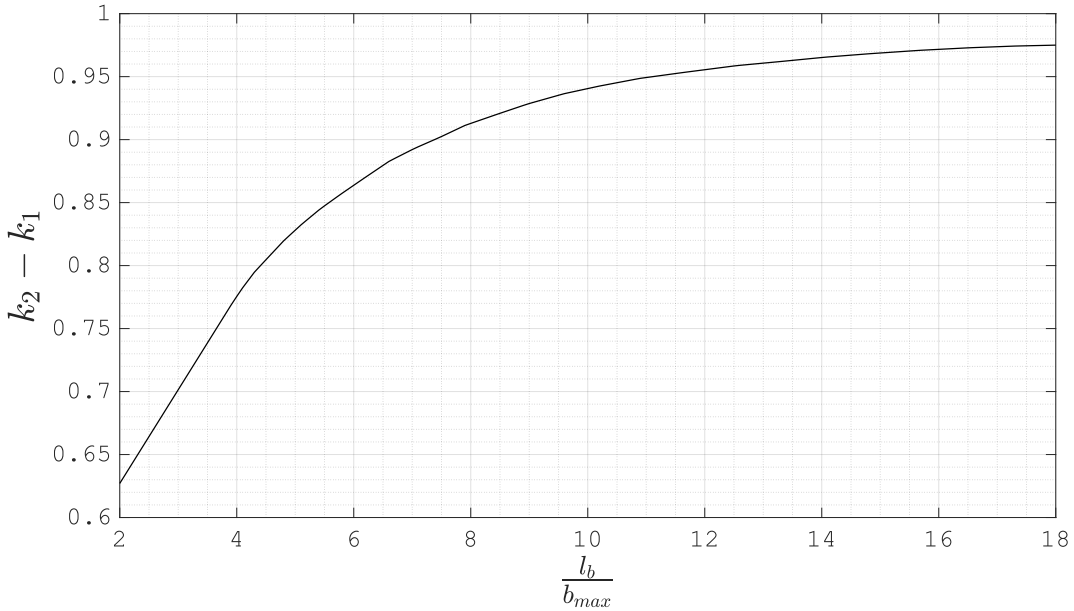

Figure 3.5: Table of values of $k_2 - k_1$

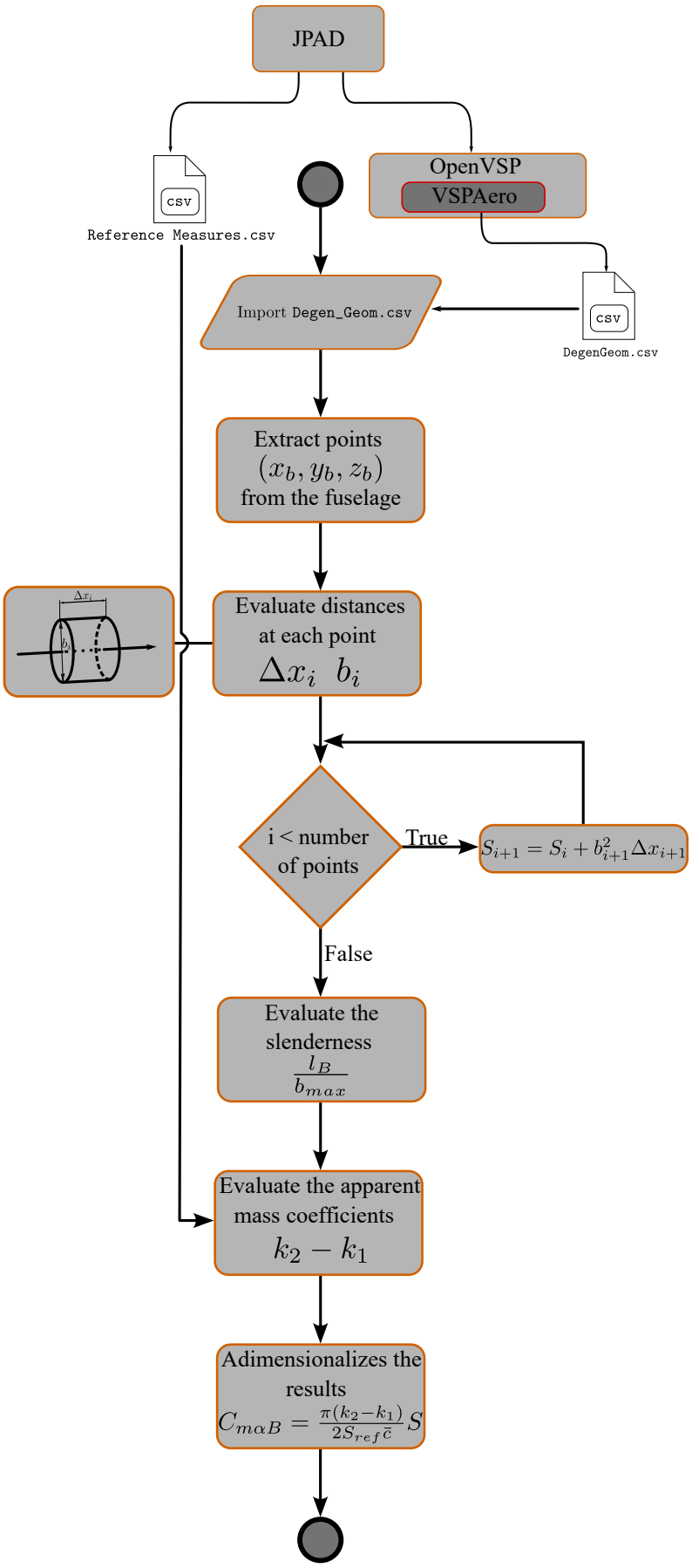

Figure 3.6: Flow chart for the program implementing the Munk method for evaluating $C_{M_{\alpha,\mathrm{B}}}$

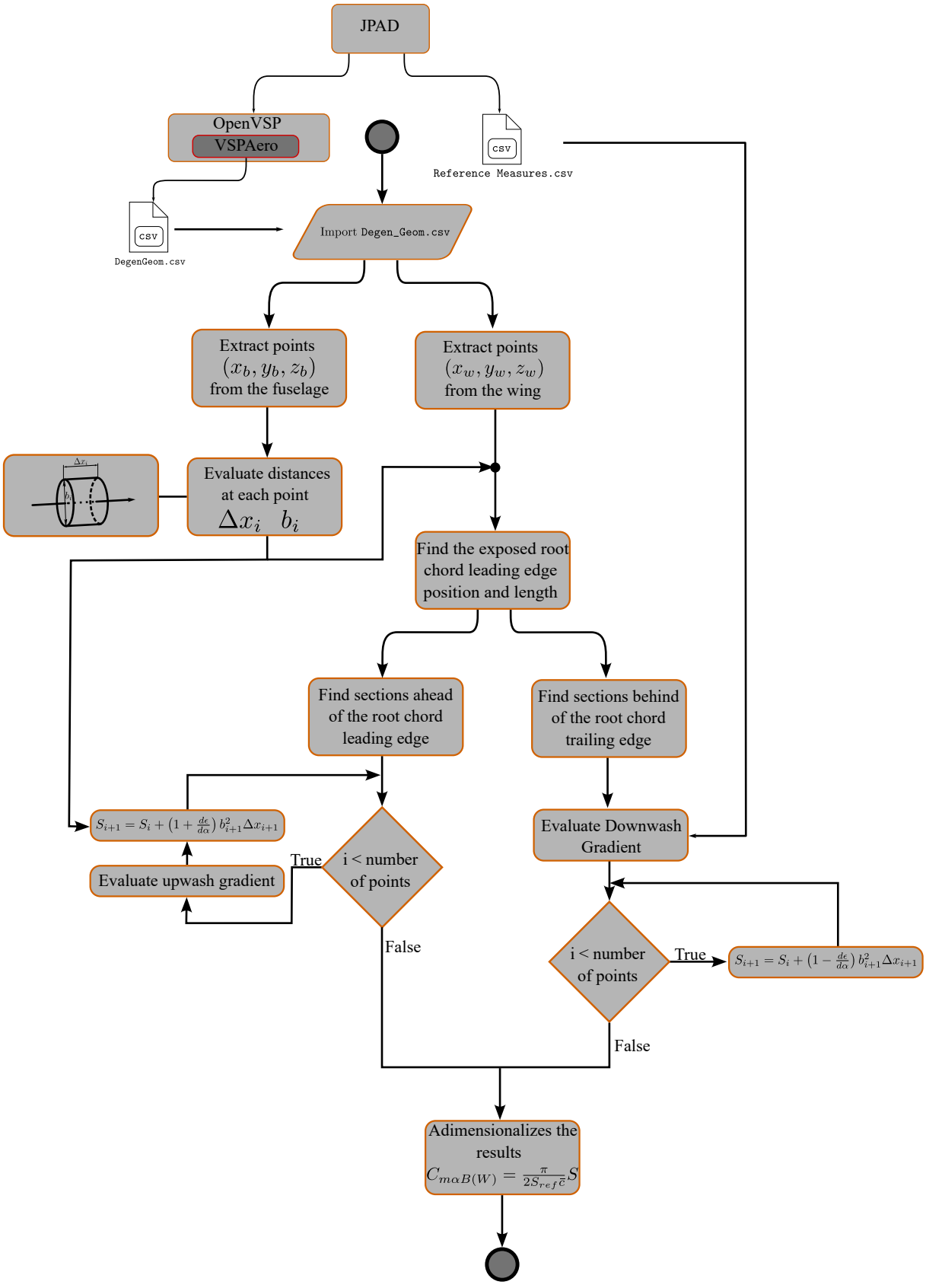

Figure 3.7: Flow chart for the program implementing the Multhopp method for evaluating $C_{M_{\alpha,\mathrm{B(W)}}}$

Chapter 4

Conclusions

The aim of this thesis was to analyse the static stability contribution of the partial configurations of all the aircraft included in the JPAD Modeller software, so that a database of moment and lift coefficients could be created. This database contains all the static stability derivatives for the longitudinal and latero-directional cases, under the assumption of small perturbations, in order to consider decoupled the longitudinal and the latero-directional motions. The raw data, consisting of values of lift and moment coefficients, were obtained from the VSPAERO solver for OpenVSP and they were post-processed with MATLAB to obtain the value of the corresponding derivatives. The results concerning the fuselage behaviour could be compared with results obtained from semi-empirical methods, relying on the same assumptions about the kind of flow field required to run the analysis within VSPAERO. A good agreement was found with the isolated body derivatives. This was not the case, though, for wing and body results, where differences between the results obtained from the two methods were significant for some cases. It must be noted that also the geometry of the airplanes was far from being completely accurate since it was approximated by the JPAD software. Some details were lost, such as the tip of the fuselage, whose points are not exported in the degenerated geometry file handled by VSPAERO. However, even the semi-empirical approaches provided large differences between their reference experiments and the equations of their methods. This was attributed to the variety of the geometries involved. Thus, VSPAERO is a valuable alternative to semi-empirical methods for the estimation of stability derivatives, especially if integrated with a geometric modeller like JPAD.

Bibliography

[1] H Multhopp. "Aerodynamics of the Fuselage". In: *Luftfahrtforschung* 18.NACA-TM-1036 (1942).

[2] Joseph Katz and Allen Plotkin. *Low-speed aerodynamics*. Cambridge university press, 2001.

[3] Max M Munk. *The aerodynamic forces on airship hulls*. Tech. rep. 1924.

[4] Joseph S. Ames. "A Rèsumè of the Advances in Theoretical Aeronauthics Made by Max M. Munk". In: *NACA Report* 213 (1926).

[5] SmartUp Engineering S.r.l. *JPAD Modeller*. 2023. URL: `https://www.smartup-engineering.com/jpad-modeller`.

[6] OpenVSP. *VSPAERO Intro and Theory*. 2023. URL: `https://openvsp.org/wiki/lib/exe/fetch.php?media=workshop23:2023_workshop_-_theory.pdf`.

[7] Jan Roskam. *Airplane flight dynamics and automatic flight controls*. DARcorporation, 1998, pp. 97–98.

[8] C.E. Pappas. "The Determination of Fuselage Moments". In: *SAE Transactions* 52 (1944), pp. 183–190.

[9] Krishnamurty Karamcheti. *Principles of ideal-fluid aerodynamics*. N.Y. R. E. Krieger Pub. Co., 1980.

Appendix

	Aircraft	X_{le} (m)	Z_{le} (m)	$x_{\bar{c}}$ (m)	$z_{\bar{c}}$ (m)	Pole coordinates x and z in m
1	A220-300	11.7	-1.25	3.78	0.509	16.45 -0.741
2	A320neo	12	-1.24	2.69	0.748	15.68 -0.492
3	A340	22.92	-1.78	7.61	1.323	32.55 -0.457
4	AN32	8.55	1.6	0.42	-0.124	9.67 1.476
5	ATR42	8.77	1.471	0.17	0	9.52 1.471
6	ATR72	11.2	1.65	0.21	0	11.99 1.65
7	B737-600	9	-0.8	3.71	0.663	13.82 -0.137
8	B737-700	10.3	-1	3.72	0.666	15.14 -0.334
9	B737-800	13.5	-0.9	3.72	0.666	18.34 -0.234
10	B737-900	15.24	-1	3.72	0.666	20.08 -0.334
11	C-130H	12	1.8	0	0	13.13 1.8
12	C-27J	7	1.5	0.13	0.098	7.84 1.598
13	Canadair CL415	7	1.72	0	0	7.88 1.72
14	EmbraerLegacy650	11.2	-0.9	2.27	0.201	14.18 -0.699
15	Falcon10x	13	-1	4.94	0.285	18.96 -0.715
16	Falcon8x	9.3	-0.9	3.6	0.213	13.7 -0.687
17	G400	9.9	-1	4.03	0.126	15 -0.874
18	G650	10.7	-1.2	4.49	0.291	16.31 -0.909
19	G700	11.8	-0.68	4.16	0.292	17.01 -0.388
20	G800	9.8	-1.1	3.95	0	14.84 -1.1
21	global6000	9.7	-1	3.57	0.269	14.24 -0.731
22	global7000	10.9	-0.9	4.61	0.257	16.6 -0.643
23	global8000	9.5	-0.9	4.44	0.347	15.03 -0.553
24	Learjet45	7.91	-0.68	0.85	0.14	9.29 -0.54
25	Praetor600	8.4	-0.9	2.69	0.372	11.69 -0.528
26	Q400	13.7	1.486	0.22	0.126	14.53 1.612
27	Regional Jet RM	16.33	-1.35	3.79	0.491	21.13 -0.859

Table A1: Positions of the Wing reference measurements

	Aircraft	$X_{\mathrm{H,le}}$ (m)	$Z_{\mathrm{H,le}}$ (m)	$x_{\mathrm{H},\bar{c}}$ (m)	$z_{\mathrm{H},\bar{c}}$ (m)	$\bar{c}_{\mathrm{H}}$ (m)
1	A220-300	33.00	1.00	1.60	0.246	2.49
2	A320neo	31.53	0.67	1.65	0	2.80
3	A340	57.98	1.79	3.67	0.453	5.42
4	AN32	20.51	1.28	0.74	0.213	2.06
5	ATR42	20.53	5.60	0.35	0	1.52
6	ATR72	25.30	5.40	0.40	0	1.65
7	B737-600	24.90	1.20	1.86	0.504	2.62
8	B737-700	24.90	1.20	1.86	0.504	2.62
9	B737-800	33.53	1.20	1.86	0.504	2.62
10	B737-900	35.97	1.20	1.86	0.504	2.62
11	C-130H	25.50	1.70	0.80	0	3.41
12	C-27J	16.00	1.55	0.64	0.042	1.83
13	Canadair CL415	17.20	3.35	0.00	0	2.42
14	EmbraerLegacy650	24.40	4.70	0.72	0	1.87
15	Falcon10x	31.80	5.10	1.60	0	2.92
16	Falcon8x	20.80	2.58	1.48	-0.133	2.16
17	G400	24.10	4.70	1.27	0	2.17
18	G650	27.60	5.40	1.76	0	2.86
19	G700	28.80	4.10	1.80	0	2.73
20	G800	27.90	5.70	1.45	0	3.08
21	global6000	24.00	4.30	1.57	-0.151	2.63
22	global7000	28.10	4.50	1.58	-0.099	2.57
23	global8000	25.50	4.50	1.58	-0.099	2.72
24	Learjet45	15.67	2.35	0.64	0	1.24
25	Praetor600	18.60	3.80	1.19	0	1.94
26	Q400	30.40	5.40	0.50	0	1.80
27	Regional Jet RM	37.80	5.80	1.42	0	2.72

Table A2: Positions of the Horizontal Tail reference measurements

	Aircraft	$C_{L_{\alpha,\mathrm{W}}}$ (10^{-2}	$C_{M_{\alpha,\mathrm{W}}}$ deg^{-1})	$\bar{x}_{\mathrm{a.c.,W}}$	$X_{\mathrm{a.c.,W}}$ (m)
1	A220-300	8.187	−1.098	0.384	16.97
2	A320neo	8.397	−0.777	0.342	16.05
3	A340	7.907	−0.948	0.370	33.52
4	AN32	8.812	−0.893	0.250*	9.67
5	ATR42	8.927	−0.166	0.250*	9.52
6	ATR72	9.075	−0.112	0.250*	11.99
7	B737-600	8.057	−0.774	0.346	14.25
8	B737-700	8.073	−0.786	0.347	15.58
9	B737-800	8.073	−0.786	0.347	18.78
10	B737-900	8.073	−0.783	0.347	20.52
11	C-130H	8.248	0.121	0.235	13.06
12	C-27J	8.394	−0.058	0.250*	7.84
13	Canadair CL415	8.332	0.125	0.235	7.82
14	EmbraerLegacy650	7.993	−0.547	0.318	14.37
15	Falcon10x	7.543	−0.653	0.322	19.26
16	Falcon8x	7.796	−0.836	0.357	14.05
17	G400	7.191	−0.635	0.338	15.38
18	G650	7.426	−0.690	0.343	16.72
19	G700	7.760	−0.479	0.312	17.26
20	G800	7.698	−0.588	0.326	15.17
21	global6000	7.761	−0.624	0.330	14.55
22	global7000	7.513	−0.608	0.331	16.95
23	global8000	7.546	−0.560	0.324	15.35
24	Learjet45	8.002	0.054	0.243	9.28
25	Praetor600	8.085	−0.652	0.331	11.88
26	Q400	9.167	0.127	0.236	14.49
27	Regional Jet RM	8.092	−0.544	0.317	21.40

Table A3: Values the lift and moment coefficients and the positions of the wing aerodynamic centre for the isolated wing

	Aircraft	$C_{L_{\alpha,\mathrm{W}}}$ (10^{-2})	$C_{M_{\alpha,\mathrm{W}}}$ (10^{-3})	$C_{\mathcal{N}_{\beta,\mathrm{W}}}$ (10^{-5})	$C_{\mathcal{L}_{\beta,\mathrm{W}}}$ (10^{-3})
1	A220-300	8.187	−10.984	−1.787	−1.530
2	A320neo	8.397	−7.767	−6.501	−1.703
3	A340	7.907	−9.481	−2.297	−1.733
4	AN32	8.812	−8.928	1.901	0.648
5	ATR42	8.927	−1.664	0.607	−0.142
6	ATR72	9.075	−1.121	0.659	−0.086
7	B737-600	8.057	−7.737	−4.513	−1.928
8	B737-700	8.073	−7.862	−7.044	−2.036
9	B737-800	8.073	−7.862	−7.044	−2.036
10	B737-900	8.073	−7.834	−7.077	−2.030
11	C-130H	8.248	1.214	0.848	0.066
12	C-27J	8.394	−0.582	−2.022	−0.856
13	Canadair CL415	8.332	1.250	0.440	0.020
14	EmbraerLegacy650	7.993	−5.472	−0.110	−1.260
15	Falcon10x	7.543	−6.534	2.474	−1.907
16	Falcon8x	7.796	−8.357	1.097	−1.538
17	G400	7.191	−6.349	2.325	−1.349
18	G650	7.426	−6.904	6.840	−2.466
19	G700	7.760	−4.794	0.723	−0.600
20	G800	7.698	−5.875	5.072	−0.923
21	global6000	7.761	−6.240	0.344	−1.702
22	global7000	7.513	−6.081	1.320	−1.322
23	global8000	7.546	−5.604	2.597	−1.671
24	Learjet45	8.002	0.539	−0.697	−0.678
25	Praetor600	8.085	−6.522	−1.778	−2.168
26	Q400	9.167	1.270	−0.122	−0.773
27	Regional Jet RM	8.092	−5.439	−0.667	−2.332

Table A4: Values of longitudinal and latero-directional stability derivatives for the isolated wings (all coefficients are expressed in deg^{-1})

	Aircraft	$C_{L_{\alpha,\mathrm{WB}}}$	$C_{M_{\alpha,\mathrm{WB}}}$	$C_{\mathcal{L}_{\beta,\mathrm{WB}}}$	$C_{\mathcal{N}_{\beta,\mathrm{WB}}}$
		(10^{-2})			
1	A220-300	8.160	1.832	1.991	−0.261
2	A320neo	8.355	1.752	1.923	−0.279
3	A340	7.943	1.023	1.021	−0.157
4	AN32	8.745	1.693	1.834	−0.140
5	ATR42	8.806	2.738	2.570	−0.223
6	ATR72	8.979	2.973	2.851	−0.228
7	B737-600	8.094	0.882	1.122	−0.196
8	B737-700	8.116	0.882	1.282	−0.215
9	B737-800	8.066	1.087	1.587	−0.266
10	B737-900	8.117	1.263	1.733	−0.289
11	C-130H	8.079	1.000	1.079	−0.155
12	C-27J	8.235	1.311	1.296	−0.244
13	Canadair CL415	8.141	1.113	1.287	−0.133
14	EmbraerLegacy650	7.911	1.108	1.401	−0.195
15	Falcon10x	7.486	0.641	0.875	−0.120
16	Falcon8x	7.712	0.872	1.275	−0.146
17	G400	7.149	0.448	0.604	−0.107
18	G650	8.849	0.542	0.664	−0.114
19	G700	7.716	0.699	0.846	−0.114
20	G800	7.663	0.605	0.734	−0.125
21	global6000	7.751	0.535	0.698	−0.110
22	global7000	7.499	0.416	0.604	−0.093
23	global8000	7.518	0.367	0.543	−0.083
24	Learjet45	7.947	1.103	1.305	−0.209
25	Praetor600	8.001	1.150	1.496	−0.172
26	Q400	9.108	2.577	2.594	−0.206
27	Regional Jet RM	8.008	1.764	2.156	−0.271

Table A5: Values of longitudinal and latero-directional stability derivatives in deg^{-1} for the wing-body configuration

	Aircraft	$C_{M_{\alpha,\mathrm{B}}}$ (10^{-2})	$C_{\mathcal{L}_{\beta,\mathrm{B}}}$ (10^{-3})	$C_{\mathcal{N}_{\beta,\mathrm{B}}}$ (10^{-5})
1	A220-300	2.364	−2.609	6.136
2	A320neo	2.298	−2.791	7.343
3	A340	1.230	−1.568	3.356
4	AN32	1.865	−1.398	6.474
5	ATR42	2.797	−2.235	9.756
6	ATR72	3.064	−2.282	6.644
7	B737-600	1.339	−1.960	4.787
8	B737-700	1.479	−2.153	5.036
9	B737-800	1.827	−2.659	5.222
10	B737-900	1.987	−2.890	5.195
11	C-130H	1.055	−1.551	7.188
12	C-27J	1.379	−2.437	14.065
13	Canadair CL415	1.226	−1.326	9.624
14	EmbraerLegacy650	1.486	−1.950	5.151
15	Falcon10x	0.962	−1.205	1.888
16	Falcon8x	1.204	−1.457	3.844
17	G400	0.658	−1.071	2.495
18	G650	0.767	−1.138	2.125
19	G700	0.964	−1.141	2.543
20	G800	0.894	−1.249	2.109
21	global6000	0.819	−1.101	2.696
22	global7000	0.677	−0.931	1.686
23	global8000	0.594	−0.825	1.666
24	Learjet45	1.336	−2.090	6.448
25	Praetor600	1.545	−1.724	5.378
26	Q400	2.722	−2.058	5.193
27	Regional Jet RM	2.302	−2.714	5.844

Table A6: Values of longitudinal and latero-directional stability derivatives in deg^{-1} for the isolated fuselage obtained from VSPAERO

	Aircraft	$C_{M_{\alpha,\mathrm{B}}}$ VLM	Munk	err.	$C_{N_{\beta,\mathrm{B}}}$ VLM	Munk	err.
		(10^{-2})		(%)	(10^{-3})		(%)
1	A220-300	2.364	2.550	7.29	−2.609	−2.771	5.84
2	A320neo	2.298	2.457	6.48	−2.791	−2.951	5.44
3	A340	1.230	1.345	8.54	−1.568	−1.652	5.14
4	AN32	1.865	1.967	5.19	−1.398	−1.424	1.85
5	ATR42	2.797	2.888	3.13	−2.235	−2.318	3.60
6	ATR72	3.064	3.267	6.22	−2.282	−2.391	4.56
7	B737-600	1.339	1.361	1.62	−1.960	−1.826	7.36
8	B737-700	1.479	1.516	2.45	−2.153	−2.024	6.37
9	B737-800	1.827	1.907	4.21	−2.659	−2.544	4.51
10	B737-900	1.987	2.084	4.62	−2.890	−2.774	4.18
11	C-130H	1.055	1.070	1.42	−1.551	−1.495	3.72
12	C-27J	1.379	1.399	1.46	−2.437	−2.518	3.23
13	Canadair CL415	1.226	1.212	1.16	−1.326	−1.260	5.21
14	EmbraerLegacy650	1.486	1.628	8.75	−1.950	−2.127	8.28
15	Falcon10x	0.962	1.048	8.28	−1.205	−1.256	4.05
16	Falcon8x	1.204	1.303	7.63	−1.457	−1.586	8.10
17	G400	0.658	0.707	7.01	−1.071	−1.147	6.66
18	G650	0.767	0.824	6.95	−1.138	−1.206	5.65
19	G700	0.964	1.033	6.70	−1.141	−1.173	2.75
20	G800	0.894	0.961	7.02	−1.249	−1.355	7.81
21	global6000	0.819	0.881	6.99	−1.101	−1.175	6.32
22	global7000	0.677	0.733	7.67	−0.931	−1.010	7.77
23	global8000	0.594	0.642	7.49	−0.825	−0.882	6.49
24	Learjet45	1.336	1.426	6.30	−2.090	−2.269	7.89
25	Praetor600	1.545	1.681	8.08	−1.724	−1.871	7.87
26	Q400	2.722	2.932	7.17	−2.058	−2.182	5.66
27	Regional Jet RM	2.302	2.483	7.30	−2.714	−2.964	8.43

Table A7: Comparison among results from the Munk method and VLM on isolated fuselage

	Aircraft	$C_{M_{\alpha,\mathrm{WB}}}$ VLM	Multhopp	err.
		(10^{-2})		(%)
1	A220-300	1.832	1.991	8.01
2	A320neo	1.752	1.923	8.88
3	A340	1.023	1.021	0.28
4	AN32	1.693	1.834	7.72
5	ATR42	2.738	2.570	6.51
6	ATR72	2.973	2.851	4.27
7	B737-600	0.882	1.122	21.36
8	B737-700	0.882	1.282	31.25
9	B737-800	1.087	1.587	31.51
10	B737-900	1.263	1.733	27.11
11	C-130H	1.000	1.079	7.34
12	C-27J	1.311	1.296	1.20
13	Canadair CL415	1.113	1.287	13.57
14	EmbraerLegacy650	1.108	1.401	20.93
15	Falcon10x	0.641	0.875	26.74
16	Falcon8x	0.872	1.275	31.57
17	G400	0.448	0.604	25.91
18	G650	0.542	0.664	18.42
19	G700	0.699	0.846	17.34
20	G800	0.605	0.734	17.56
21	global6000	0.535	0.698	23.30
22	global7000	0.416	0.604	31.09
23	global8000	0.367	0.543	32.46
24	Learjet45	1.103	1.305	15.45
25	Praetor600	1.150	1.496	23.14
26	Q400	2.577	2.594	0.67
27	Regional Jet RM	1.764	2.156	18.16

Table A8: Comparison among results from the Multhopp method and VLM (in deg^{-1}) on the body under the aerodynamic interference of the wing

	Aircraft	C_{M_W} 10^{-1} at α, deg				
		0	2.5	5	7.5	10
1	A220-300	−1.226	−1.455	−1.719	−2.017	−2.317
2	A320neo	−0.837	−0.986	−1.170	−1.366	−1.617
3	A340	−1.277	−1.482	−1.708	−1.959	−2.223
4	AN32	−0.048	−0.033	−0.042	−0.076	−0.132
5	ATR42	−0.022	−0.010	−0.033	−0.093	−0.189
6	ATR72	−0.039	−0.020	−0.034	−0.077	−0.150
7	B737-600	−1.658	−1.851	−2.042	−2.235	−2.433
8	B737-700	−1.660	−1.849	−2.046	−2.241	−2.447
9	B737-800	−1.660	−1.849	−2.046	−2.241	−2.447
10	B737-900	−1.660	−1.846	−2.045	−2.240	−2.442
11	C-130H	−0.088	−0.055	−0.023	0.006	0.033
12	C-27J	−0.071	−0.048	−0.050	−0.077	−0.129
13	Canadair CL415	−0.084	−0.050	−0.017	0.014	0.040
14	EmbraerLegacy650	−1.262	−1.404	−1.544	−1.683	−1.806
15	Falcon10x	−1.523	−1.672	−1.808	−1.931	−2.076
16	Falcon8x	−1.682	−1.905	−2.114	−2.319	−2.519
17	G400	−1.362	−1.527	−1.684	−1.848	−1.995
18	G650	−1.687	−1.871	−2.038	−2.210	−2.380
19	G700	0.001	−0.122	−0.243	−0.362	−0.478
20	G800	−1.685	−1.840	−1.984	−2.125	−2.277
21	global6000	−1.650	−1.821	−1.986	−2.135	−2.274
22	global7000	−1.146	−1.304	−1.461	−1.607	−1.755
23	global8000	−1.568	−1.717	−1.855	−1.996	−2.129
24	Learjet45	−1.393	−1.380	−1.373	−1.358	−1.337
25	Praetor600	−1.622	−1.794	−1.963	−2.124	−2.273
26	Q400	−0.051	−0.016	0.017	0.047	0.076
27	Regional Jet RM	−1.601	−1.744	−1.881	−2.023	−2.142

Table A9: Values of C_{M_W} in deg^{-1} at different angles of attack